May 2014

Theoretical Model and Test Bed for the Development and Validation of Ornithopter Designs

Alexandra Lee Beando
Worcester Polytechnic Institute

Christopher William Overton
Worcester Polytechnic Institute

Jesus O. Chung Mock
Worcester Polytechnic Institute

Kevin Mauricio Ramirez
Worcester Polytechnic Institute

Tyler Ayanna Pietri
Worcester Polytechnic Institute

Theoretical Model and Test Bed for the Development and Validation of Ornithopter Designs

A Major Qualifying Project Report
Submitted to the Faculty of the
Worcester Polytechnic Institute
In partial fulfillment of the requirements for the
Degree of Bachelor of Science
By

Alexandra Beando

Christopher Overton

Tyler Pietri

Jesus Chung

Kevin Ramirez

Date: May 1, 2014

Approved By:

Professor Marko Popovic

Professor Stephen Nestinger

Abstract

Ornithopters, biomimetic systems that utilize flapping wing flight to generate lift, are a growing field of robotics. Large scale ornithopters have several real world applications, including payload carrying and transport. Although these bio-inspired robots are of particular interest, there are currently no successful large scale hovering ornithopters in existence over 2 kilograms. Continuing from last year's MQP, this project developed a prediction and validation system that can effectively guide, examine, and validate ornithopter prototype designs. The system includes a theoretical model and a test bed. The model is based on the kinematic chain used in Active Lab's hummingbird ornithopter prototype and founded in flapping wing aerodynamics. The theoretical model thus serves to project the performance outcomes of ornithopter prototype designs prior to construction. Using the model's predictions, a physical ornithopter prototype was created for the project. The test bed was used to analyze the ornithopter and validate the theoretical model predictions. Utilizing load cells, cameras, and a LabVIEW interface, the test bed allows for the hard mounting of different ornithopter designs and the examination of different wing designs and wing motion.

Acknowledgments

We'd like to acknowledge our project advisors, Professor Popovic and Professor Nestinger, for their continual guidance, wisdom, and patience throughout the project. We would also like to extend our gratitude to Hydrocutter, Inc. for providing free water jet services and materials for our chassis and Cabrillo College for their pixel tracking software, Tracker, which was used in our analysis.

Table of Contents

Table of Figures

Table of Tables

Table of Authorship

Chapter	Author(s)	Primary Editior	Secondary Editor
Chapter 1	Tyler Pietri	Alexandra Beando	Tyler Pietri
Chapter 2	Tyler Pietri	Alexandra Beando	Tyler Pietri
Chapter 3	Jesus Chung, Christoper Overton	Tyler Pietri	Jesus Chung
Chapter 4	Jesus Chung, Christoper Overton	Tyler Pietri	Jesus Chung
Chapter 5	Tyler Pietri	Alexandra Beando	Tyler Pietri

Chapter 1: Introduction

Ornithopters, biomimetic robotic systems, utilize flapping wing flight to generate and sustain lift. In his book, *Biomechanics and Robotics*, Marko Popovic describes flapping wing models as more energy efficient in both takeoff and sustained flight than prevalent fixed-wing and rotary-wing flight mechanisms. The increase in efficiency is mainly due to interactions between the airfoils and drag forces. In fixed wing models, the system must gain speed until the lift forces overcome the drag. By comparison, ornithopters actively utilize and manipulate drag to generate and sustain lift. An added benefit of flapping wing systems is their improved power-to-weight ratio, allowing them to produce more power at significantly reduced weight than fixed wing or rotary wing models. This is particularly beneficial for vertical takeoff and landing, or VTOL (Popovic, 2013).

Although ornithopters may offer increased efficiency, the science behind them is more complex and significantly less understood than their alternatives. This issue is neatly summarized by Muller and DeLaurier who note that though "the propulsive efficiencies of large ornithopters match the best that propellers can give, the additional complexity of such aircraft do not currently make them competitive with fixed wing designs (Mueller, 2001)." Despite this disadvantage, there are a number of significant real world applications for ornithopter robotic systems. These include endurance flight, stealth-by-mimicry for security and surveillance, payload carrying, and most notably, increased in-flight maneuverability and efficiency (Grauer and Hubbard, 2009). The many potential benefits of ornithopters make them worthy of further research. Several researchers have attempted to address this through the creation of ornithopter specific test platforms and test bed vehicles. Three examples of this can be seen in the University of Maryland's Odyssey (Morpheus Labs, 2010), the Flapping-Wing Micro Air Vehicle (FWMAV) (Sahai, et. al, 2012) and the Slow Hawk (Doncieux et. al, 2011).

The Odyssey is an ornithopter prototype created by the Morpheus Laboratory of U. Maryland's A. James Clark School of Engineering. The prototype, which weigh 350 grams and has a 1.2 meter wingspan, serves as a "test bed vehicle" for the examination of flapping wing flight dynamics. As the vehicle flies, it collects

a range of data including; pitch, roll, yaw, center of gravity, and airfoil flap frequency and inertial forces. The vehicle is able to do this through the integration of a custom built avionics board into its design. The board features gyroscopes, accelerometers, and magnetometers; sensors which allow measurements to be taken on-board the odyssey as it engages in flight and then downloaded from a removable memory card once testing is completed (Morpheus Labs, 2010).

The second test platform is the one used on the Flapping-Wing Micro Air Vehicle (FWMAV) developed in 2012 by R. Sahai et. al, this FWMAV is a modular, small scale ornithopter prototype of 156 millimeters in wingspan and just under 15 grams in total weight. To examine the flight dynamics of the prototype, Sahai et. al built a static test platform on which the FMWAV could be hard mounted. The platform itself features a 6-axis force sensor, an encoder, and a 420 fps high speed video camera. Information is collected real time through a National Instruments data acquisition board and processed in its accompanying LabVIEW software (Sahai et. al, 2012). Similar to the FWMAV is the DelFly autonomous ornithopter created by Netherland's Delft University of Technology. Like the FWMAV the DelFly is also a flapping wing micro air device, but rather than being a simple prototype, it is a self-contained test bed vehicle. Built into the DelFly are wireless microcontrollers, analog cameras gyroscopes, and pressure sensors. These allow for wireless collection of flapping wing dynamic data. The only aspect of the DelFly test bed that is not integrated into the vehicle itself is a Particle Image Velocimetry (PIV) system on which the device can be hard mounted to analyze the air flow field generated by airfoil flapping (G.C.H.E. DeCroon, et. al, 2009).

Unlike the three prototypes mentioned earlier, the Slow Hawk is a commercially available ornithopter RC toy of 510 grams in weight and 150 centimeters in wingspan. AnimatLab, a Parisian bio robotics research center, uses the device to conduct air flow experiments via a wind tunnel test platform. The information gained is used to validate an in-house flapping wing physical stimulator (Doncieux et. al, 2011).

While all of these test beds and test bed vehicles are successful in collecting data, they are all somewhat limited. In the Odyssey and DelFly designs, the test platform is physically integrated into the ornithopter prototype and moves along with the device as it engages in flight (Morpheus Labs, 2010), (G.C.H.E. DeCroon, et. al, 2009). This type of platform design severely restricts overall usability and functionality.

New ornithopter prototypes cannot be interchanged into the test bed; rather a new series of sensors and testing mechanisms would need to be incorporated into the ornithopter. This is time consuming and dissuades rapid prototype creation and analysis. By comparison, the FMWAV uses a static test bed on which the prototype can be hard mounted and analyzed (Sahai et. al, 2012). Though this is a marked improvement which allows for interchangeability of prototype designs, the FWMAV is ultimately a micro air vehicle and some of its test bed features may not be applicable to large scale ornithopter designs. While the Slow Hawk used by AnimatLabs address the issues of interchangeable large scale ornithopter testing, it is used in wind tunnel experiments (Doncieux et. al, 2011). A wind tunnel sized to fit a large scale ornithopter is prohibitively expensive and unconducive to transportation. In light of these issues, this project focuses on the creation of a transportable, static test platform on which large scale ornithopter prototypes can be interchanged and analyzed.

In addition to research on ornithopter prototypes and test beds, this project was partially inspired by the 2013 MQP, "Toward Biologically Inspired Human-Carrying Ornithopter Robot Capable of Hover" (Deisadze et. al, 2013). Desisadze et. al aimed to create a large scale ornithopter capable of VTOL and hover. This aim was realized in the form of a plain steel, spring loaded prototype of 29 kilograms in weight and 3.2 meters in wingspan. Though the device managed to achieve some lift, approximately 7 centimeters of bounce under tethered conditions, the group faced several limitations with their device; particularly notable, were the issues with prototype design and accurate data acquisition. Video data from "Tether Flapping Tests 4 and 5" reveal the prototype could not produce consist lift, had asynchronous airfoil flapping, and as a whole, was too cumbersome and hazardous to be effectively tested (Deisadze et. al, 2013).

To address those issues, this project sought to create a theoretical model and test platform for the prediction, construction, and validation of ornithopter designs. Given a set of input variables, the theoretical model predicts the power requirements and expected performance outcomes of ornithopter designs. The information gained can be used to alter and improve ornithopter prototypes prior to construction, thus avoiding some of the issues faced by the 2013 MQP group. Once the prototype is built, its predicted

performance outcomes can then be validated through a test bed. The test bed is used to directly capture lift, velocity, and position data and allows for interchangeability of large scale ornithopter designs. In this way, the test bed addresses the limitations of existing test bed vehicles such as the Odyssey, the FMWAV, and the DelFly. This paper will review the design, development, and results of the prediction and validation system.

Chapter 2: Project Strategy

This chapter discusses the formation of the project goals, the approach to reach said goals, and the project's design parameters.

2.1 Project Goal

As mentioned earlier, the project was motivated by the work of the 2013 Ornithopter MQP team. Although, the 2013 team managed to create a large scale ornithopter, their work was limited by issues with prototype design and accurate data acquisition. Based on this, the 2014 project advisors communicated a desire to construct a framework for ornithopter development from which a reliable prototype could be built and analyzed. A review of the 2013 Ornithopter MQP's analysis methods revealed that both lift and position data were extrapolated from the prototype based on its position in selected still frames from a video recording (Deisadze et. al, 2013). While this technique may be suitable to determine wing position and height, it is inappropriate for lift analysis as it allows for the introduction of both bias and error into the data. Due to the lack of appropriate testing measures, it was determined that a testing mechanism for ornithopter prototypes would need to be developed in addition to the creation of a framework for ornithopter design. Upon consideration of these issues, the project goal was established as follows:

"To devise a theoretical model and test bed for the development, construction, and examination of flapping wing based flight prototypes."

Based on the goal, the project called for the creation of three separate components: a theoretical model, an ornithopter prototype, and a test bed. The theoretical model provides the framework the development of ornithopter designs, the physical prototype provides a device on which to conduct numerical studies, and the test bed allows for the analysis of the prototype and the validation of the theoretical model. A

comprehensive system of this nature for large scale ornithopters does not currently exist and was of significant interest to the project advisors for its potential to further ornithopter research.

2.2 Design Parameters

The following design parameters were used to guide project development.

Overall Parameters:

1. Cost

   The total cost of the theoretical model, ornithopter prototype, and test bed may not exceed USD $750.00

Theoretical Model Parameters:

1. Functionality:
   - The theoretical model must be input customizable and allow for the performance prediction for any desired ornithopter weight, dimension, or angle of attack
   - The theoretical model must be able to predict expected ornithopter prototype lift and airfoil flapping frequency for a given set of input variables.

Ornithopter Prototype Parameters:

1. Weight:
   - The prototype cannot exceed 10kg in total weight
2. Dimension:
   - The prototype chassis must be no larger than 1.5m in either width or length and cannot exceed 12cm in height.
   - The prototype airfoils may be no larger than 1m in either length or height.
3. Functionality:
   - The prototype must allow for synchronous flapping of the airfoils.

- The prototype must allow for interchangeable airfoils.
- The prototype must be powered by an electronic speed controller (ESC), RC Transmitter, and receiver.

Test Bed Parameters:

1. Weight:
    - The test bed sensor platform must be no more than 2.5kg in total weight
2. Dimension:
    - The test bed's sensor platform cannot exceed 1m in either length or width and can be no larger than 12cm in height.
3. Functionality:
    - The test bed must be its own separate entity and cannot be physically integrated into the ornithopter prototype.
    - The test bed must allow for interchangeable force sensors to allow for the incorporation of higher rated sensors for heavier ornithopter prototypes.
    - The test bed must provide hard mounting locations that fully constrain the ornithopter prototype in the x, y, and z axes.
    - Test bed construction and breakdown should not exceed 20 minutes.
    - The test bed must be able to collect lift, wing orientation, and wing velocity from a constrained ornithopter prototype.

Chapter 3: Methodology

This chapter is divided into three sections that match the goals set for the project. Section 4.1 outlines the theoretical model, how it was modeled and considerations that were taken into account for the mechanical design. Section 4.2 describes the steps taken in manufacturing and creating the ornithopter prototype based upon considerations from the theoretical model. Finally, Section 4.3 shows in detail the test bed used to analyze the physical prototype and validate the theoretical model. It should be noted that hereafter, the term airfoils will be referred to as wings.

3.1 Theoretical Model

A theoretical model is a description technique which applies mathematical and scientific concepts to engineering disciplines for the purpose of explaining systems, studying the effects of different components within the system, and predicting component behavior. Theoretical modeling is a highly beneficial pre-prototyping measure that allows for a better understanding of the needs and capabilities of a system's physical model prior to construction. This concept was utilized to aid in the creation of the ornithopter prototype component of the test platform. By creating a model and simulation in MATLAB (MathWorks, 2014), the parameters and limitations of various ornithopter designs were clearly demonstrated. Figure 1 shows the prototype diagram used to model the system.

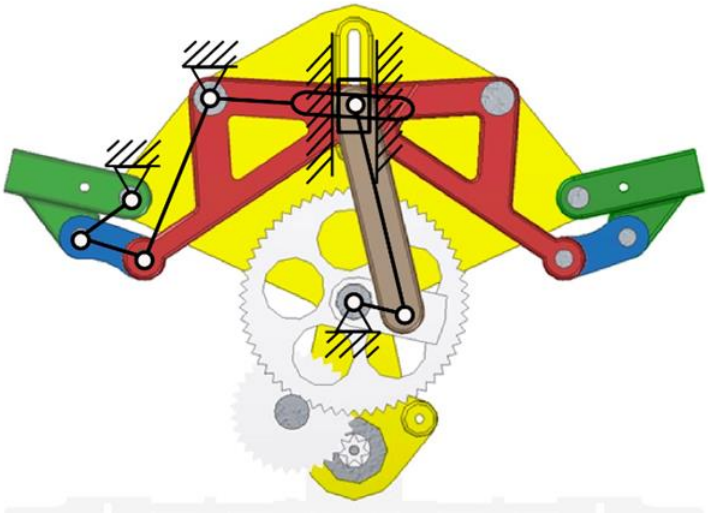

Figure 1: The Active Structures Flapping Mechanism (Karasek, 2011).

3.2 Mechanical Modeling

The ornithopter's proposed design utilized an electric motor to transfer power to the wings and thus produce lift. For this reason, most of the theoretical modeling focused on the mechanical system that transfers that power. To simplify the model, the system was divided into three subsections; the drive mechanism (slider-crank and motor), the double rocker mechanism, and the wing component.

The Newton-Euler algorithm describes the combined translational and rotational dynamics of a rigid body. It relates the motion of the center of gravity of a rigid body with the sum of forces and torques acting upon it (Ardema, 2005). For this model, the forward recursive Newton-Euler algorithm was used to determine the Cartesian position and velocities of each component by calculating them recursively as a function of joint angles from the base frame of reference up to the wing tip. The forces and torques at each segment could be calculated through utilizing the back recursive Newton-Euler algorithm.

A series of known variables within the sub-sectional components of the ornithopter assisted in the modeling. To begin, the slider-crank four bar linkage converts the rotational motion of the motor into linear motion that moves the wings. The velocity and position of the slider can be determined through knowing the motor's speed. The next component is the double-rocker four bar linkage. This linkage amplifies the angular

displacement of the wing relative to the slider-crank's linear movement from the slider-crank by two-fold. This mechanism also serves as the pivot position and shoulder joint for wing motion. Finally, the wings are modeled as flat plates with a given attack angle during the forward and backstroke. Detailed analysis of these components can be seen in Appendix ##.

The overall goal in creating a theoretical model to acquire an understanding of the lift forces acting on the ornithopter. Accordingly, known aerodynamic concepts for lift of a fixed plate were incorporated within the model to assist in analyzing these forces. By understanding the kinematics of actuation, the transmission of force from the motor to the wing was tracked. An understanding of the typical forces was developed using the equations for lift.

3.2.1 Aerodynamics of Flapping Wing Flight

As detailed in Figure 2, the wings were modeled as flat plates moving within the horizontal plane. By comparison to more complex flapping modes such as the humming bird figure eight style, using a flat plate simplified the modeling assumption significantly.

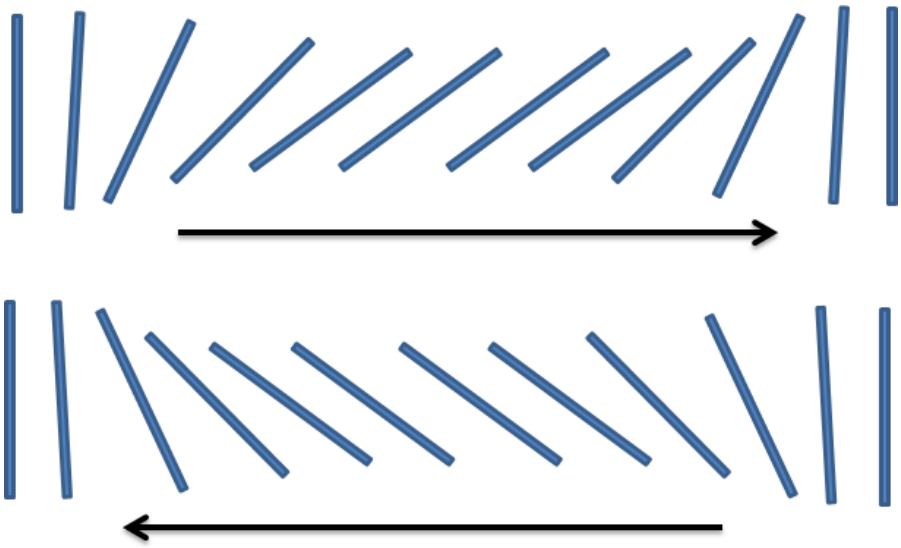

Figure 2: Wing motion for horizontal flapping. Arrow shows direction of wing movement.

$$F = \frac{1}{6} * C_d * \rho * \sin\gamma * \cos\gamma^2 * \Omega^2$$

Some of the assumptions taken into account were:

1. The wings remain rigid throughout the flapping motion.
2. There is a constant angle of attack throughout the flapping motion.
3. There is no friction between the wings and the fluid.

3.3 Ornithopter Design

The results of the theoretical model, as seen in Appendix B, drove the approach to the mechanical system design of the ornithopter prototype.

3.3.1 Design and Manufacturing

The prototype consists of a symmetrical four-bar linkage design that serves as an amplifier to obtain high amplitude flapping motion, and is driven by a slider crank based mechanism that generates a low amplitude rocker motion. The subcomponents with their detailed analysis are described in detail in Appendix C.

Figure 1 shows the mechanism on which the prototype was based. The Active Structures Laboratory at Université Libre De Bruxelles in Belgium used this same flapping mechanism prototype for a project to develop a hummingbird-like flying robot (Karasek, 2011). The four-bar linkages provides a strong mechanical advantage. The long driven link in the four-bar magnifies the torque output at a cost of range of motion.

Using the concept shown in Figure 1, a prototype design was created that met the desired range of motion and output force as calculated in the theoretical model, Appendix B. Figure 3 shows the CAD model of the prototype. Each component of the mechanism was water jet out of 3.175mm (0.125”) aluminum sheet. The components were then drilled to size and the edges cleaned.

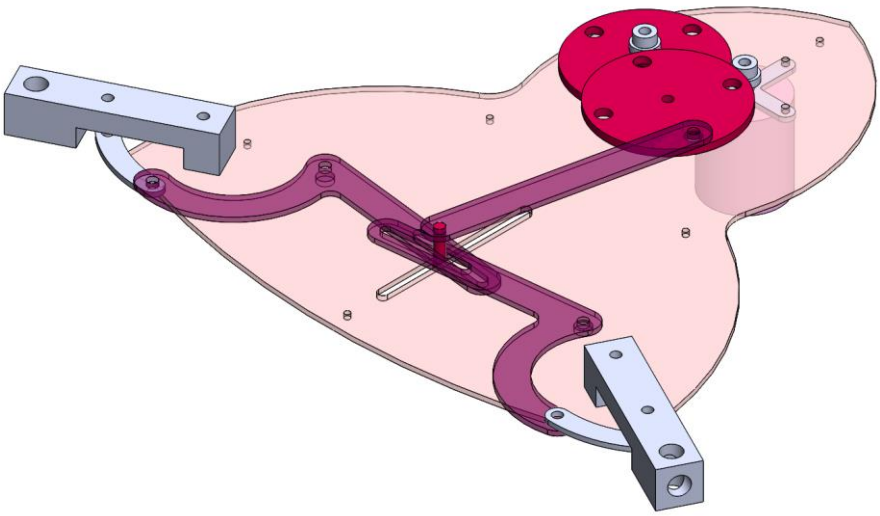

Figure 3: Prototype Design

3.3.2 Shoulder Design

The shoulders allow the user to test different wing designs easily through a slot-pin design. There are intersecting 0.5” holes drilled into the end and top through to the bottom as seen in Figure 4. This allows to easily change wings by a simple pin mechanism, which fully constrain the wing.

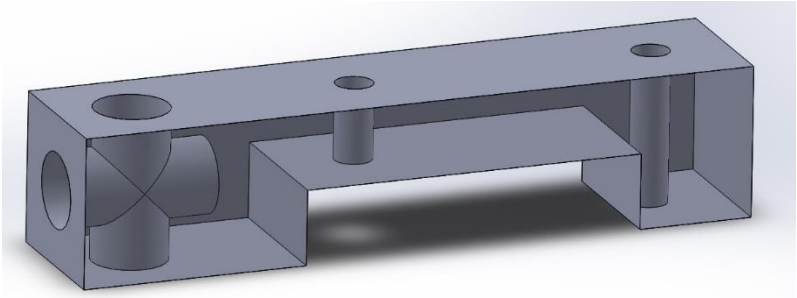

Figure 4: Internal View of Shoulder Joint Design

3.3.3 Drive Mechanism

The motor used in the prototype design is a Tacon Bigfoot 46 Brushless motor powered (HobbyPartz, 2013) by HobbyWing Platinum-80A-PRO Brushless Electronic Speed Controller (ESC) (HobbyPartz, 2014). The motor is 670kv at 22.2V and at maximum power draw, would turn at 14,874rpm. To transfer the power from the high-RPM motor to the crank-slider mechanism, a two stage gearbox configured for a

30:25:1 gear reduction was needed. After the gear reduction, the maximum output speed of the mechanism would be approximately 8 Hz.

3.3.4 Wing Design

The wings are made of three components as shown in Figure 5, the wing material or "skin", the top bar of the wing or "bone", and the vertical bar, or "post". The skin was made of Nylon, a synthetic polymer, because of its durability, high elongation and resilient (Palmer, 2001). The post was made of a 10in. aluminum rod that weighed 2.98oz. The bone was made of three different materials in different experiments. An aluminum rod that weighed 7.995oz, an oak wooden dowel that weighed 3.07oz, and a carbon fiber tube that weighed 2.45oz. All bars measured .5in. x 30in.

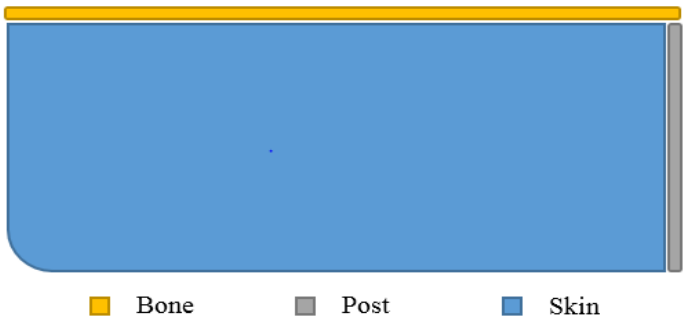

Figure 5: Simplified View of Wing Components

Figure 6: Wing Design Iterations (please edit images for background consistency)

Figure 6 shows the wings from a front view. As seen in the upper image of Figure 6, the first iteration of the wing design included 2 struts attached to the skin of the wing at a 30^{o} angle with the bone. This design was intended to give structural support to the pocket formed during wing motion. When this design was tested, however, the struts flipped over top of the bone tangling the wing and producing no lift. The second iteration had a single strut rigidly attached to the end of the bone to constrain 3 sides of the skin. This design worked well in producing a relatively even pocket as the wing passed through the air. This design was used to gather the data on the sensor platform. In both iterations, the skin of the wing was sewn out of ripstop nylon. Different bone materials were also substituted in with varying results. Originally the bones were made from aluminum rods, these were then substituted for wood dowels and finally carbon fiber tubes. Plugs were machined to fit into the ends of the carbon fiber bones in order to provide support for connection to the shoulders. The iterations of the wing serves as an example of the modularity of

the shoulder design. When each iteration was tested, the process to attach a new wing design was simple and required no modification to the existing system.

3.4 Test Platform Design

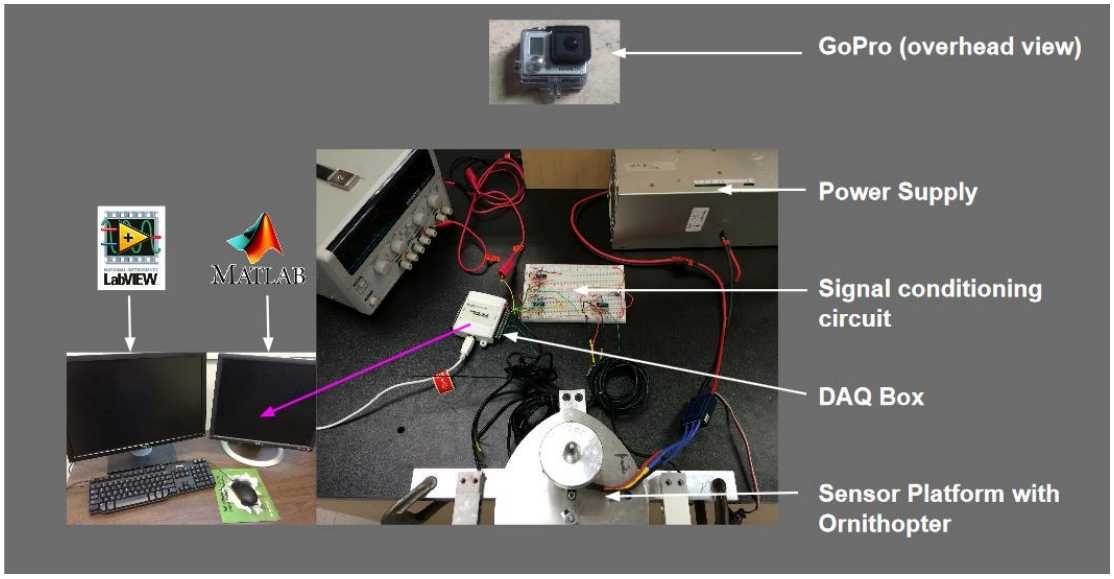

Figure 7: Overview of Test bed Setup

The final design of the test bed can been seen in Figure 7**Error! Reference source not found.**. The bed itself includes the sensor platform, the ornithopter accompanied by its voltmeter and 24V power supply, the differential amplifier referred to as the signal conditioning circuit, the NI USB-6008 DAQ box, and the computer used to process the LabVIEW (National Instruments, 2014) and MATLAB software (MathWorks, 2014).

3.5 Experimental Setup

Performance metrics were necessary to compare and validate the theoretical model with the physical ornithopter prototype. The performance metrics selected were; power required by the mechanism, angular position and velocity of the wing, as well as the force of lift created by the ornithopter. The experiment setup was built to accurately and effectively measure these metrics.

3.5.1 Electrical Power from Motor

The electrical power drawn by the motor provides the input power used by the ornithopter prototype during operation. To calculate this, both the input voltage and resulting current were measured. The voltage power supply was constant throughout the experiment, while the current was measured using a Hall Effect current sensor, ACS759 (Allegro, 2014). As can be seen in the photo below, the sensor was attached in between the electric speed controller and the motor's power supply. Following the testing methods of Wissa et. Al., the current sensor was attached in series between the power supply and the electric speed controller (Wissa et. al, 2012). Data measured by the current sensor was recorded using a simplified LabVIEW program.

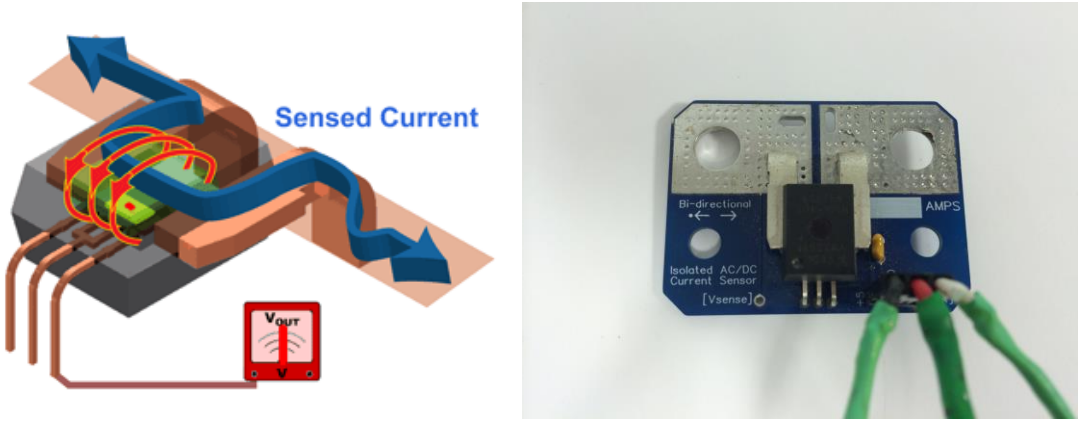

Figure 8: Hall-Effect Current Sensor

3.5.2 Angular Position and Angular Velocity of the Wing

The angular position and angular velocity of the wing tip were important metrics for prototype comparison with the theoretical model. To gather this data, a GoPro (GoPro, 2014) running at 120 fps was mounted on the ceiling. This provided a helpful top-down view of the ornithopter. The data acquired from the camera was processed using Tracker, an open source video analysis and modeling tool (Douglas, 2014). Figure 9 below details the camera setup as seen from the Tracker software.

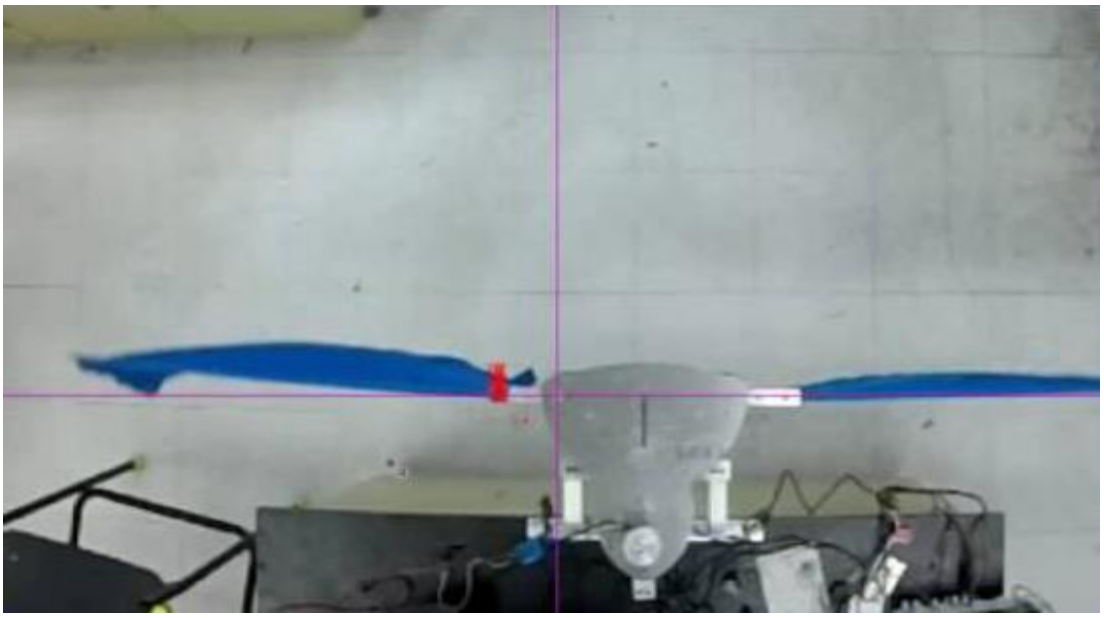

Figure 9: Top-down GoPro view as seen with red color marker within Tracker Software

Because Tracker operates by following a specific pixel cloud, a distinct color marker was placed on the ornithopter as shown in Figure 5. The marker was originally located on the end tip of the wing bone; however, it was later moved to the shoulder joint to improve marker recognition within the video tracking software. Although the equation does not account for bending within the rods, it approximated the wing tip angular velocity.

3.5.3 Lift Forces

Several sensor platform designs were conceptualized in a bid to measure the lift forces produced by the ornithopter. As the main purpose of the platform was to calculate the forces in the z-direction, it was determined that both direct and indirect measurements could be used. Direct measurements included using a force plate, whereas indirect measurement required measuring the displacement of the robot in the z-direction. Because equipment for direct measurement could not be obtained, it was decided that indirect measurement techniques would be used via the application of load cells. An early iteration of the sensor platform design incorporated two load cells attached in parallel. These served to constrain the ornithopter

from moving in either the x or y planes and measure displacement solely in the z direction. A CAD file of the early design can be seen in Figure 10.

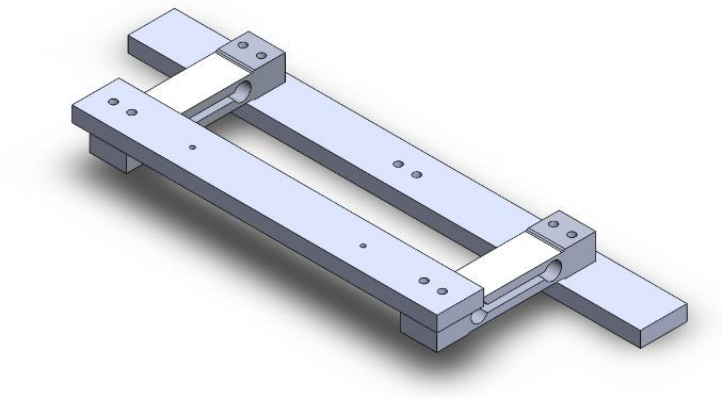

Figure 10: Early iteration of sensor platform with two parallel load cells.

These load-cells, each rated for a maximum weight of 10kg, were connected through a custom-built amplifier to accurately measure voltage changes between -10V to +10V. Figure 11 below shows the differential amplifier circuit built for each strain gauge. This circuit has a total gain of 520 to one. The data was then gathered with a NI USB-6008 data acquisition board (DAQ) integrated with LabVIEW (National instruments, 2014). To make the test bed useable, two separate programs were created in LabVIEW. The first was used to calibrate the load cells. Load cells operate by displacing under force, or loading, which can be measured as a change in voltage. Using known weights, the correlation between the force applied to the load cells and the resulting voltage displacement could be determined via the standard line equation $y=mx+b$. The second program recorded the voltage output from each load cell into a *.csv file. Figure 11shows the circuit diagram and integration with the load-cells.

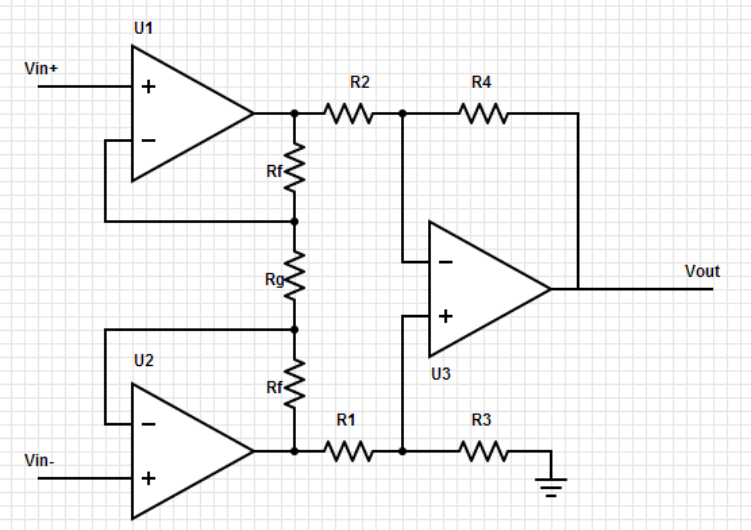

Figure 11: Electrical schematics of amplifying circuit used for each load cell.

Vin+ and Vin- are the positive and negative signals respectively, from the load cells. The output V_{out} is related to V_{in} as follows:

$$V_o = (V_{in+} - V_{in-})(R_4 + R_2)\left(\frac{2R_f}{R_g + 1}\right)$$

In order to obtain a gain of ~3700, the resistors are chosen to be the as follows $R_1 = R_2 = 10k$, $R_3 = R_4 = 100k$, $R_g = 2k$, and $R_f = 51k$.

Initial experimentation on the test platform revealed a key issue with the system's design. Data acquired via the platform contained excessive noise and was not providing accurate measurements of lift. Further experimentation determined that the noise was caused by z-directional torque generated as the center of mass (COM) changed during ornithopter operation. In order to decouple the moments generated, a third load cell was incorporated in the platform and attached to the upper most section of the ornithopter prototype's chassis. The third load cell served to decouple the moments generated during operation and calculate the forces acting on the whole system. Figure 12details the final sensor platform design with the three load-cells in a triangular array while Figure 13 shows how the ornithopter hard mounts to the uppermost load cell.

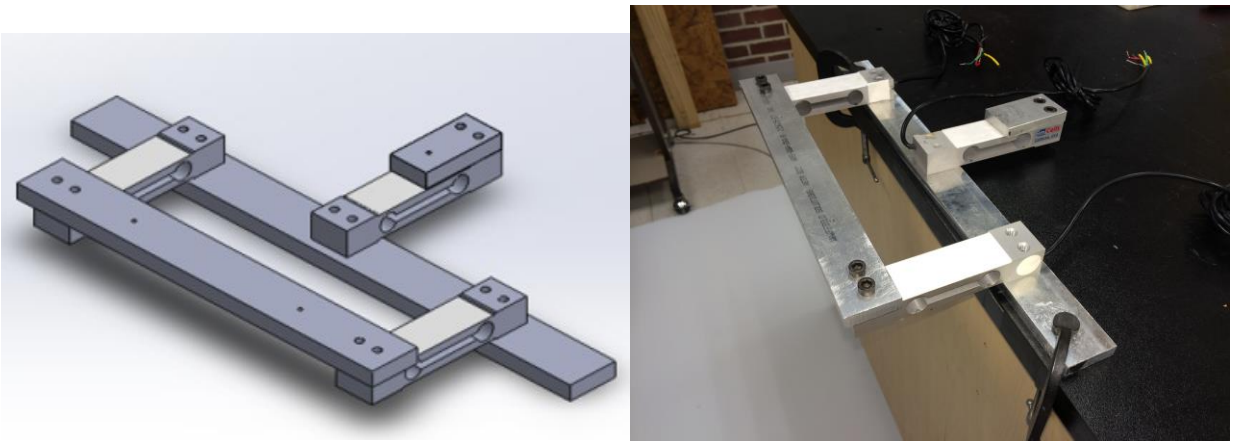

Figure 12: Sensor platform CAD model outlining the mounting points and load cell array. Left – CAD Model. Right – Sensor Platform

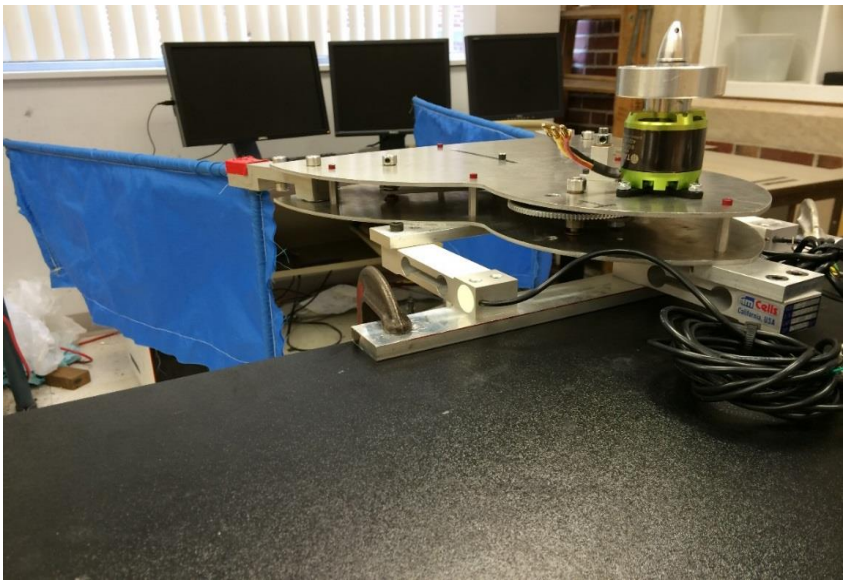

Figure 13: Side view of ornithopter prototype hard mounted to the sensor platform

For the sensor platform to accurately measure the forces acting on it, two calibrations were run to determine the linearity of the system. The calibrations were done using known weights at 2.5lbs increments. Figure 14 shows the calibration setup used for our load cell array.

Figure 14: Force Calibration setup of load cell array with known weights.

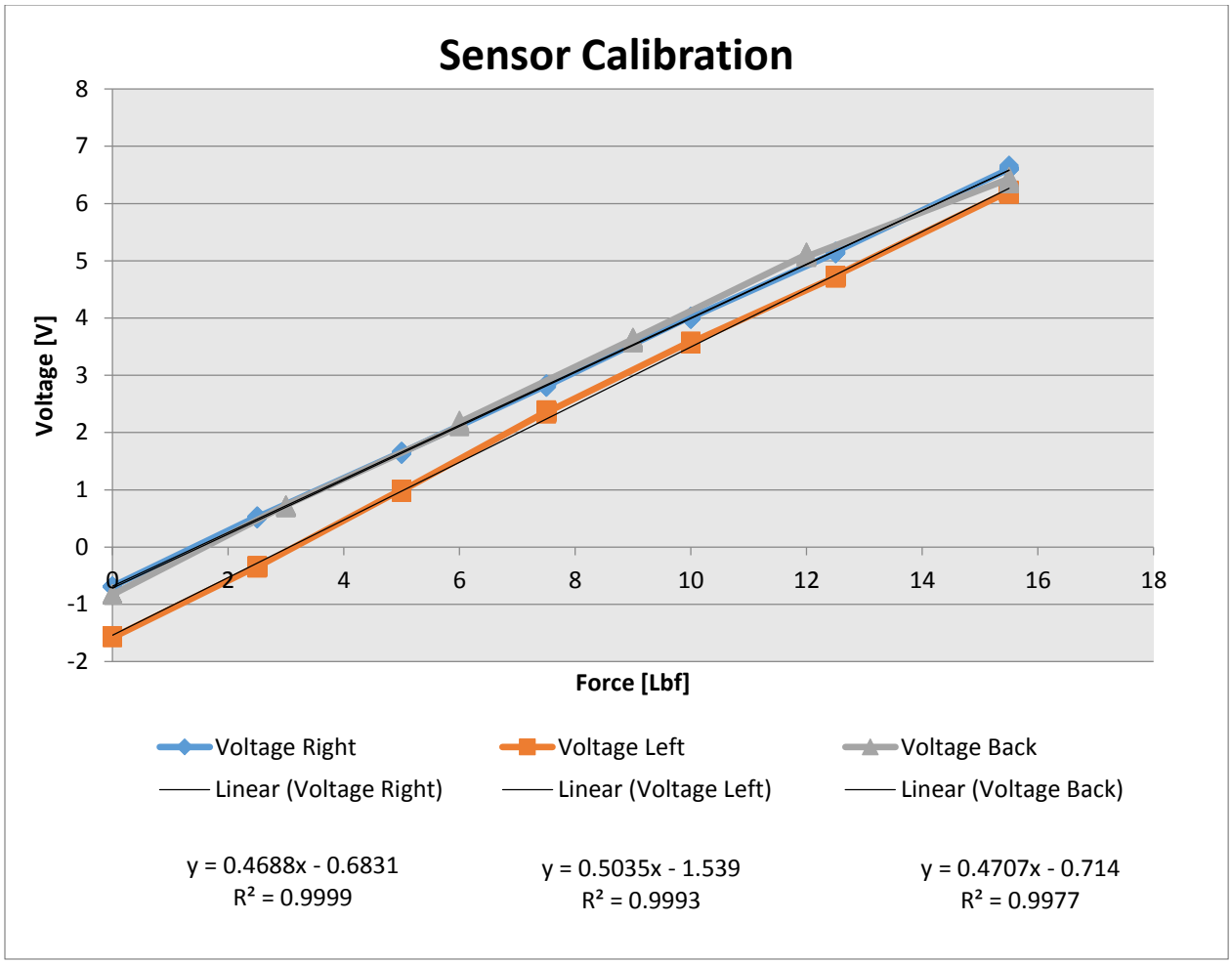

Figure 15: Sensor calibration curve with linear fit.

The first calibration was performed for each individual load cell, thus determining the linearity of each sensor and their distinct relationship between applied force and voltage output. Figure 15 shows the calibration of each individual sensor and the linear fit for each. The second calibration was performed by actuating all the sensors at the same time. Knowing the forces measured by each sensor, known weights were applied and compared. Figure 16 shows the calibration of the combined sensor data. This allows for an effective understanding of the total force generated during ornithopter prototype operation.

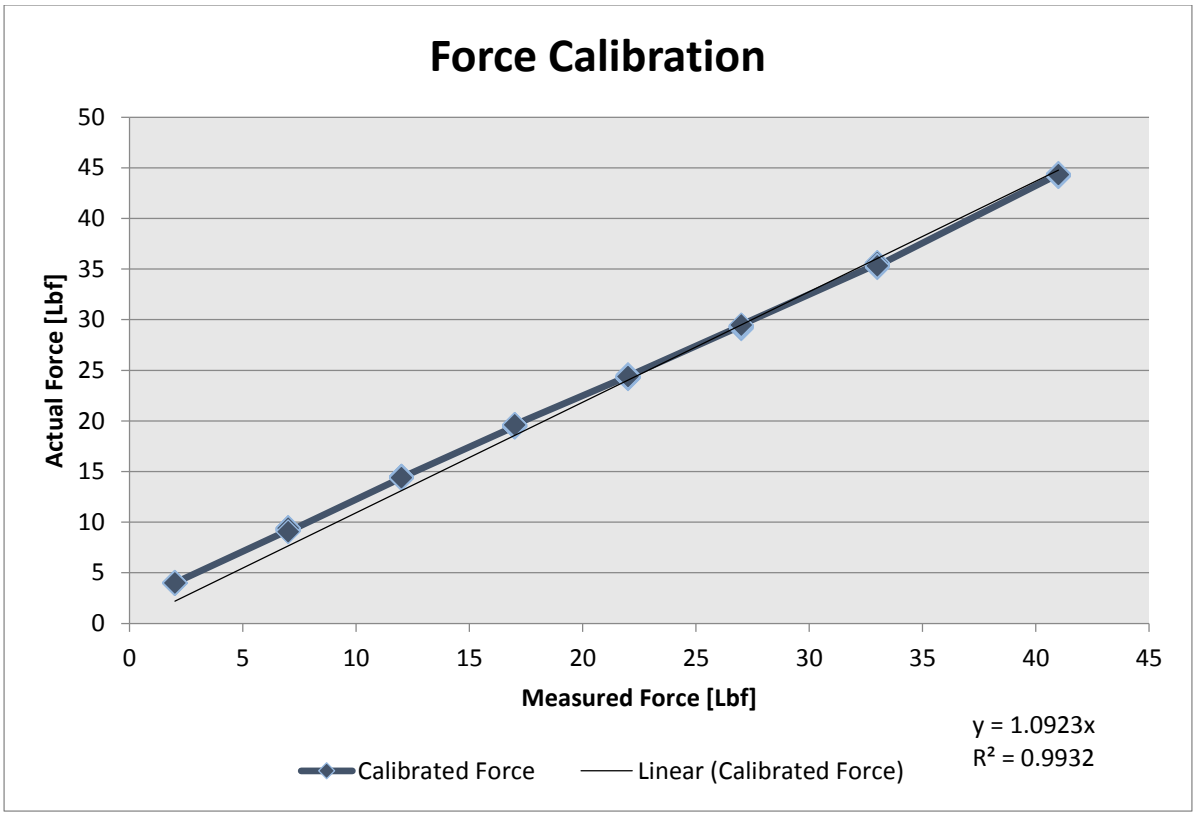

Figure 16: Combined calibration of load cell sensors with linear fit

Chapter 4: Results and Discussion

This chapter reviews the results and analysis from both the theoretical model and physical prototype. The results were derived from test runs of the ornithopter prototype and were analyzed to validate or disprove the theoretical model.

4.1 Theoretical Model

Figure 17 shows the link parameters and the dimensions associated with each. Using these dimension as given, the wing specifications could be varied in order to achieve maximum lift force from the system.

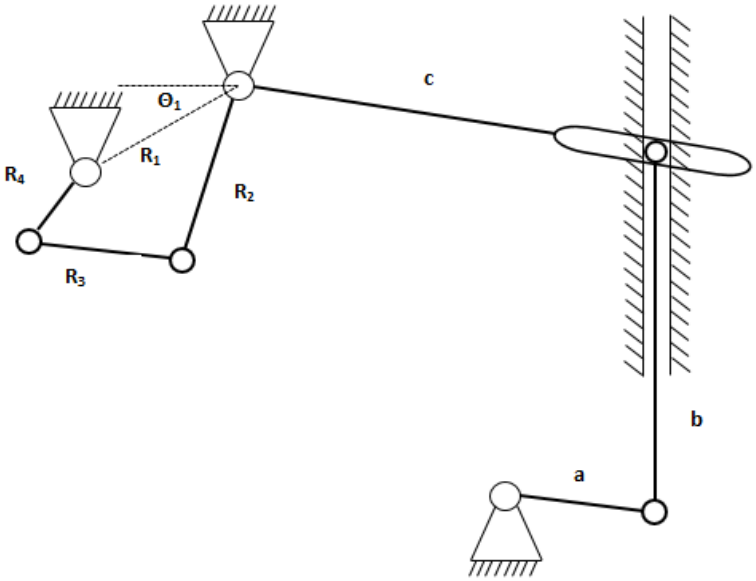

Parameter	Dimension
A	1.375”
B	6”
C	1.45”
R1	2.5”
R2	3.5”
R3	2”
R4	2”
Θ1	30°

Figure 17: Linkage parameters used in theoretical model of ornithopter design

The model was run using the values for the wing specifications and crank speed as shown in Table 1 below.

Variable	Value
Width	10”
Length	30”
Angle of Attack	30^{o}
Crank Speed	350 RPM

Table 1: Values used in theoretical model

From the model, input power (800 W) requirements as well as expected lift forces (2.81 lbf) and flapping frequency (2 Hz) were calculated.

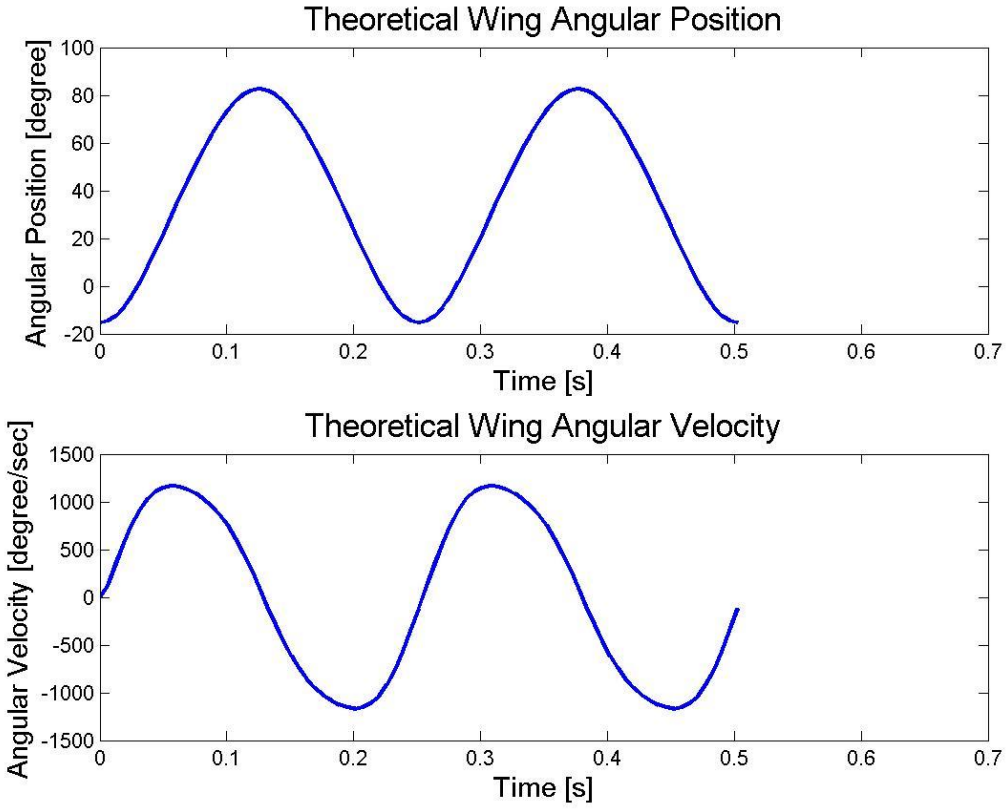

Figure 18: Theoretical Angular Position and Velocity of Wing at an input of 240rpm.

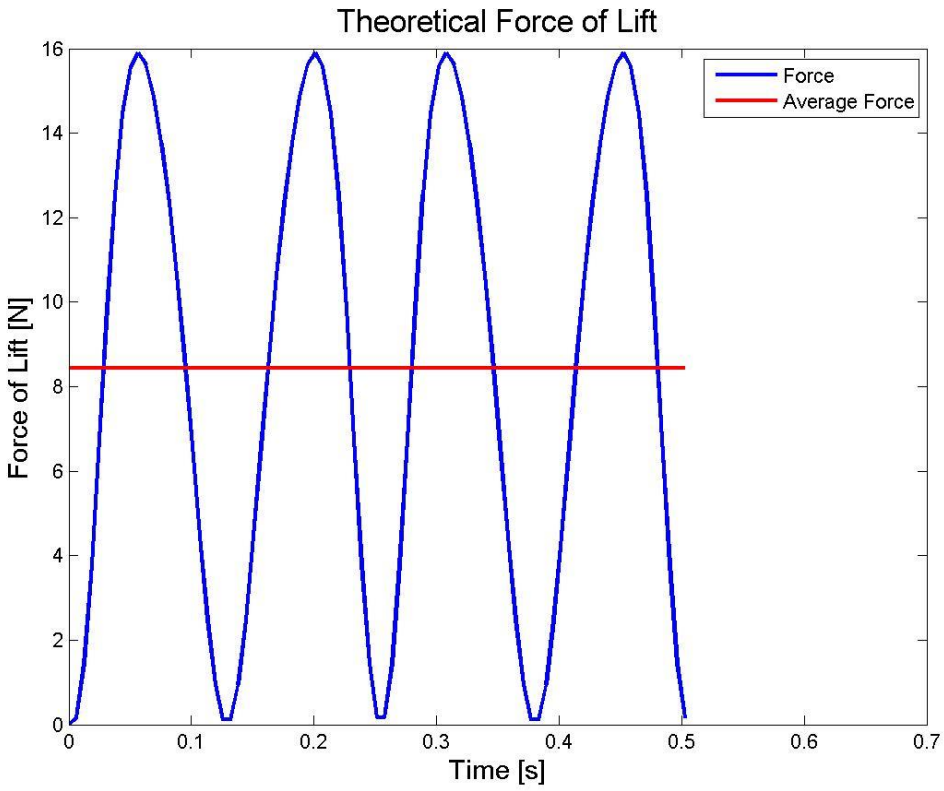

Figure 19: Theoretical Lift Force for an input crank of 240rpm.

4.2 Experiments: Performance and Results

Experimental data was collected via the sensor array and GoPro (GoPro,2014) camera of the test bed. To determine the versatility of the test bed, experiments were performed using different wing designs and materials. Two wings designs were used, the strut and 3-side fixed iterations can be seen in Figure 6, and three materials were used for the wing bone: aluminum rods, wooden dowels, and carbon fiber tubes. Because the aluminum rods were filled down to create plugs for the carbon fiber tubes before the completion of the final sensor platform design, there is no data from this material. The sensor array and video data acquired from these test will be discussed in the upcoming sections.

After running the first round of tests, the motor was visibly slowing under the inertial load of the wings changing directions. To help the motor overcome this load, a flywheel of 2.2oz in weight was added to the motor. This served to smooth the motion of both the motor and the system.

4.2.1 Sensor array data

Data from the sensor platform was collected and analyzed in MATLAB for each wing boning material (MathWorks, 2014). The wing data was then calibrated and filtered using two filters, a Low-Pass filter and a Savitzky-Golay filter. The Low-Pass filter served to eliminate general noise from the data, while the Savitzky-Golay filter was used to find the average lift force data. The filter served to remove high frequency noise and smooth the data set. Savitzky-Golay filters function by fitting polynomials to each frame of the data, thus minimizing the least-squares error and reducing noise. These filters are a better alternative to moving averages, as they screen out significant portions of a given signal's high frequency content along with the noise. In Figure 20 through Figure 24, the blue line denotes the complete filtered data, while the green line denotes the average lift force calculated using the Savitzky-Golay filter.

The graph shown in Figure 20 is the lift force data that was measured when experimentation was performed using wooden dowels as the boning of the ornithopter wings. As denoted by the peak of the average lift force line the highest measurement of lift force using wooden dowels was 1.82 lbf.

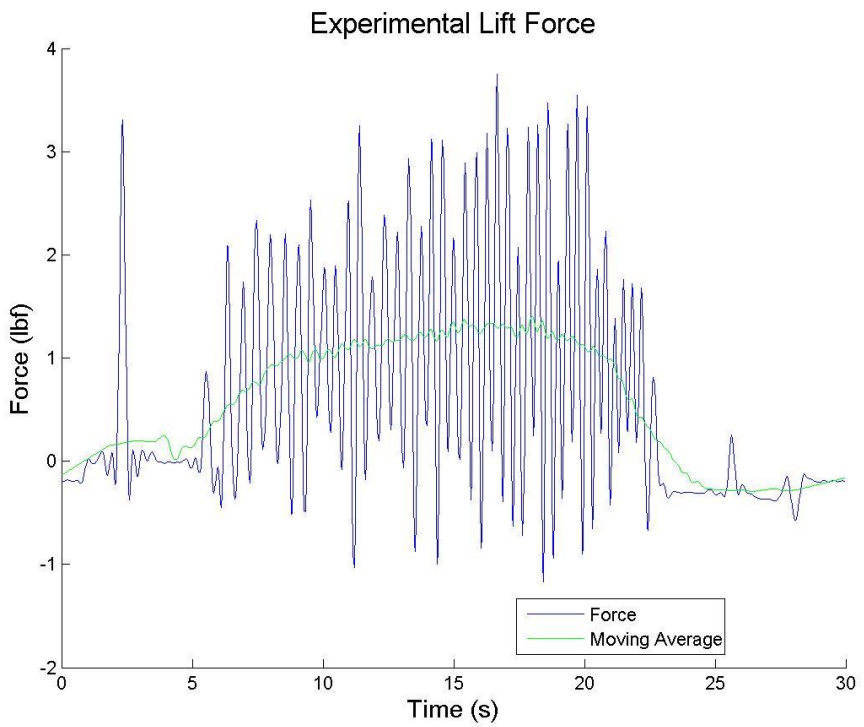

Figure 20: Lift force using wooden dowels.

Figure 21 details a two second timeframe view of Figure 20 above. The peak lift force measurement of 1.82lbf is more obvious.

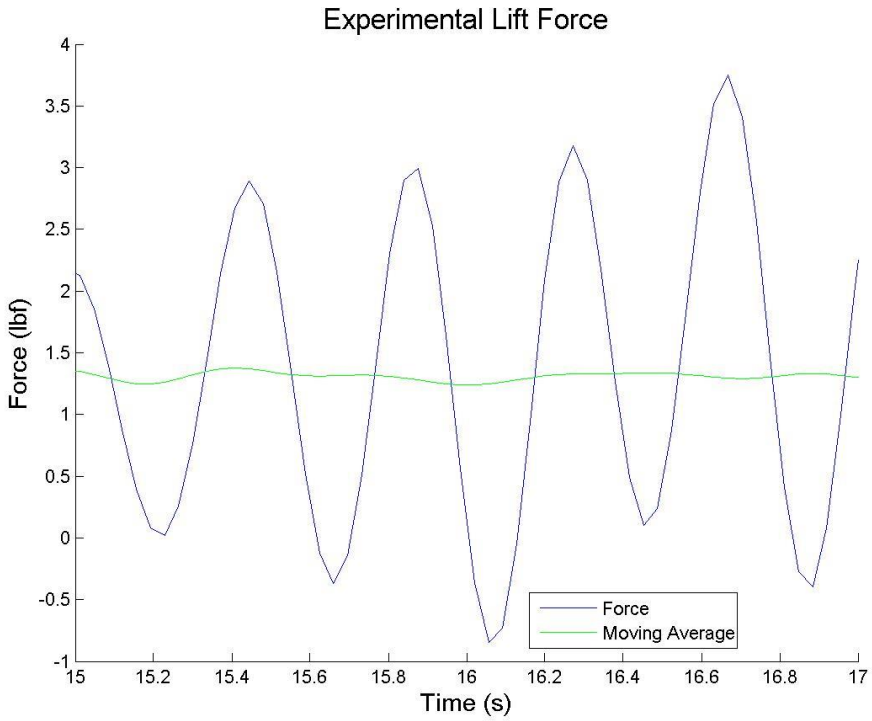

Figure 21: View of lift data using wooden dowels over a two second time interval.

A second experiment was performed using carbon fiber tubes as the wing bone material. The material properties of carbon fiber resulted in a slight decreases in weight of both the wings and the ornithopter prototype overall. As displayed in Figure 22, the maximum acquired lift using carbon fiber wing bones was determined to be 3.88 lbf. The carbon fiber tubes showed a marked improvement in getting a larger measurement of lift force. The two second timeframe view, seen in Figure 23, zooms in on the peak measurement.

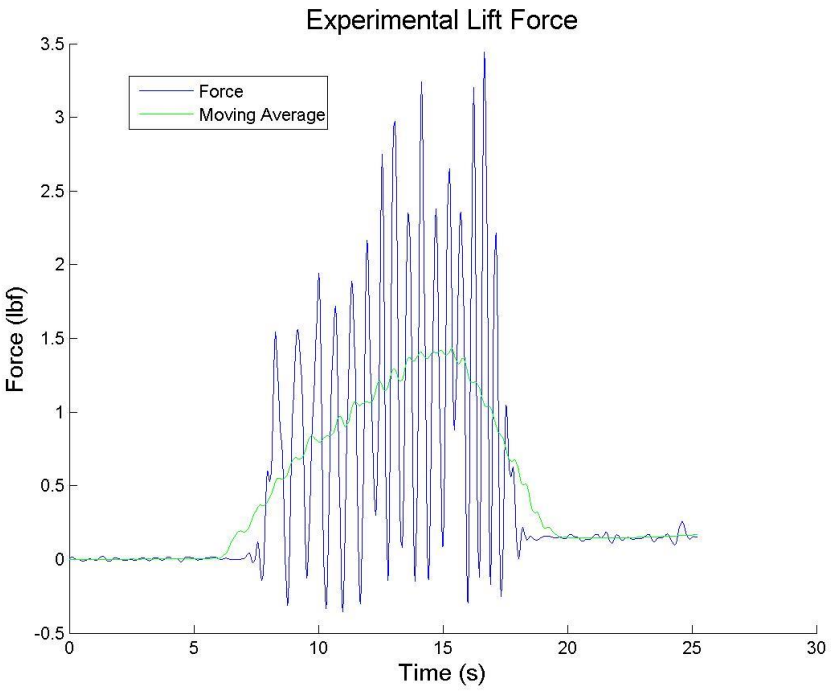

Figure 22: Lift force data using carbon fiber tubes as wing bone material

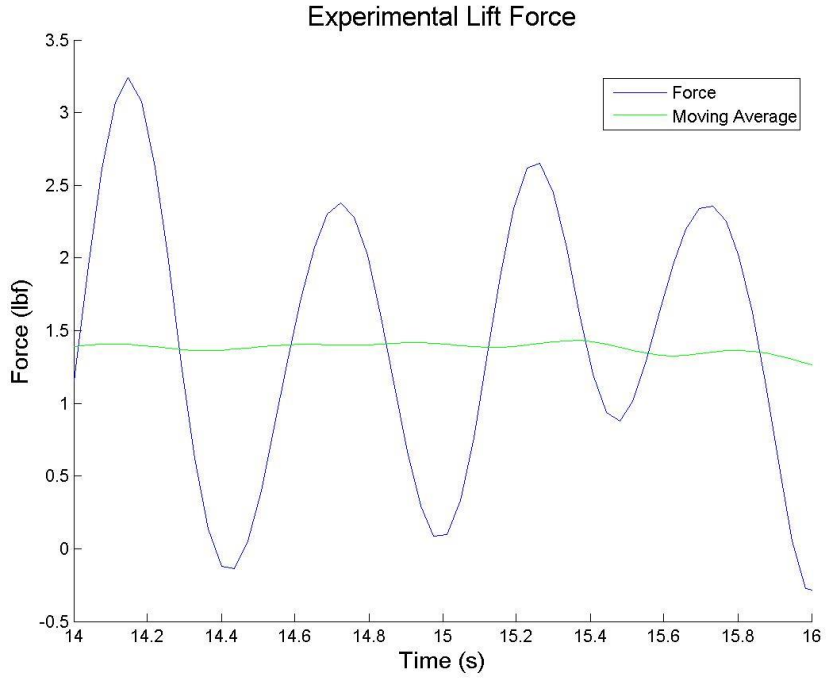

Figure 23: Two second lift force data with carbon fiber tube

Lift force data was successfully collected by separately testing the two different wing bone materials for the ornithopter prototype. The carbon fiber tubes gave the best performance, exceed the maximum lift of wooden dowel wing bones by 2.06lbf.

4.2.2 Video data

The Angular position and velocity of the wings was determined using video. The ornithopter was filmed using a high speed overhead GoPro camera (GoPro, 2014) and processed in Tracker, a pixel tracking software (Douglas, 2014). To track the position of the ornithopter wings during operation, a red color marker was placed on the shoulder joint. Figure 24 below details the angular position and velocity of the wings over a two second time window.

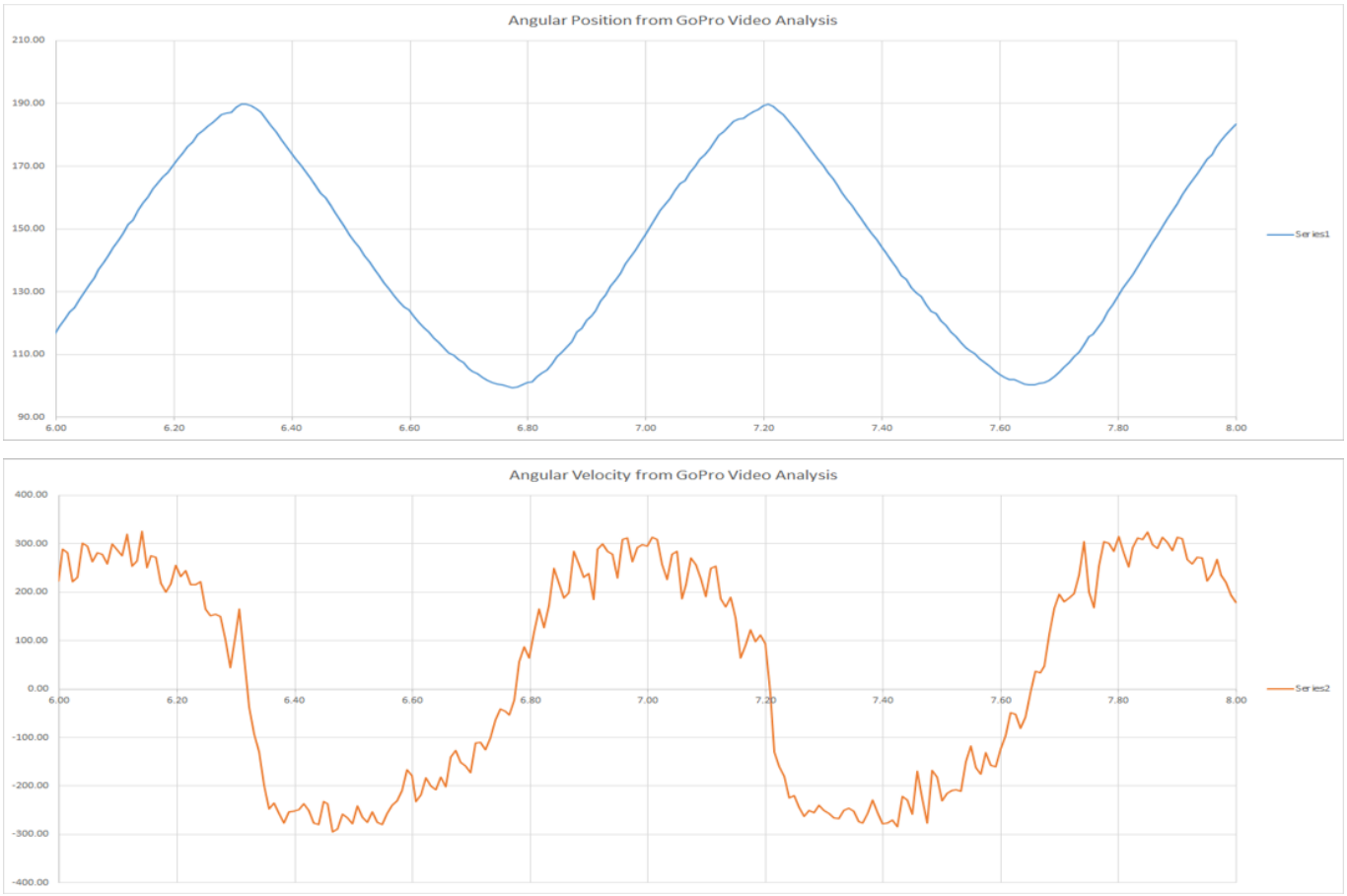

Figure 24: Two second timeframe view of video data from the tracker. Top: Angular position of the wing. Bottom: Angular velocity of the wing.

Chapter 5: Conclusions and Recommendations

5.1 Conclusions

In summation, the goal of this project was to create a prediction and validation system for the guidance, analysis, and validation of ornithopter prototype designs. The goal was realized in the form of a theoretical model and test bed. Based in aerodynamic principles and the kinematic mechanism used by Active Structures (Karasek, 2014) lab, the theoretical model was used to predict the performance outcomes of an ornithopter prototype. In particular, by using customizable input variables of angle of attack, crank speed, and wing size, the projected lift force, flapping frequency, and power requirements of the prototype could be determined. From the theoretical model's prediction, a physical ornithopter was built. The ornithopter featured a modular shoulder joints that allowed for interchangeable wing designs and materials. The test bed was then used to validate the real performance outcomes of the ornithopter prototype to those projected by the theoretical model. The test bed featured a sensor platform composed of three load cells in a triangular array and an overhead camera. Using these components together, the test bed was able to collect lift and wing position and angular velocity data which could then be analyzed in LabView (National Instruments, 2014) and MATLAB (Mathworks, 2014).

5.2 Recommendation

For a potential expansion on this project, the following improvements are suggested.

Reduce the number of assumptions within the theoretical model.

The theoretical model made several assumptions which, after experimentation, proved to be unreflective of the ornithopter prototype's actual flight dynamics. To begin, it was assumed there was no friction within the ornithopter prototype or between the surface of the wings and the air. It

was also assumed that the wings were rigid, when in actually, video data proved the wings were quite flexible; particularly with the application of more favorable low weight, low density wing bone materials. Reducing the number of assumptions within the theoretical model would improve the accuracy of its predicted performance outcomes and allows for better understanding and controlled manipulation of ornithopter prototypes.

Using a Streaming Camera for real time video acquisition and analysis.

The current test bed uses an app controlled overhead GoPro camera (GoPro, 2014). While the GoPro accomplished the basic needs of high speed video collection for wing position and velocity analysis, it was not a fully integrated component of the test bed setup. While this was not an overwhelming issue, it did make matching the timestamps between the video and the sensor platform data cumbersome. Using a streaming camera would allow the video data to be collected in real time with matching timestamps. This would allow for in-depth analysis of the relation between lift force and angular position and velocity. The inclusion of a secondary streaming camera located parallel to the prototype would allow for examination of lift force as relates to the changing shape of the wing.

Design the ornithopter prototype with a focus on weight and friction reduction.

The current ornithopter design could be improved considerably. The bulk of the ornithopter prototype's weight is contained within the chassis. The current chassis design is made of 0.125" thick sheet aluminum. Weight could be significantly reduced by incorporating a hole-pattern in to the chassis. Consideration should also be given to substituting the chassis material all together. Granta Design's CES EduPack software (Granta, 2014) may be useful in revealing a material suitable for this purpose. Friction could also be considerably reduced in future ornithopter prototypes. The current iteration uses bushings to assist with rotating components. Using roller bearings would smooth flapping motion significantly. It may also be useful to be reduce the amount of metal on metal contact between more general moving components, for example, the top and bottom of the shoulder joint and the inside surface of the ornithopter chassis.

References

Ardema, Mark D.. *Newton-Euler dynamics*. New York: Springer, 2005. Print.

“Allegro ACS759: Hall Effect-Based Linear Current Sensor”. *Allegro MicroSystems, LLC.* Web. 1 May 2014. < http://www.allegromicro.com/en/Products/Current-Sensor-ICs/Fifty-To-Two-Hundred-Amp-Integrated-Conductor-Sensor-ICs/ACS759.aspx>

Brown, Douglas. "Tracker Video Analysis and Modeling Tool ." *Tracker Video Analysis and Modeling Tool for Physics Education*. Cabrillo College, n.d. Web. 28 Apr. 2014. <https://www.cabrillo.edu/~dbrown/tracker/>.

Croon, G.c.h.e. De, K.m.e. De Clercq, R. Ruijsink, B. Remes, and C. De Wagter. "Design, aerodynamics, and vision-based control of the DelFly." *International Journal of Micro Air Vehicles* 1.2 (2009): 71-97. Print.

Deisadze, Nicholas, Woo Chan Jo, and Bo RimSeo Seo. "Toward Biologically Inspired Human-Carrying Ornithopter Robot Capable of Hover." *WPI*. Worcester Polytechnic Institute, 22 Apr. 2013. Web. 29 Apr. 2014. <http://www.wpi.edu/Pubs/E-project/Available/E-project-042613-114244/unrestricted/Wing_MQP_Report-2013-04-27_final.pdf>.

Doncieux, StÃ©phane , Jean-baptiste Mouret , Laurent Muratet, and Jean-arcady Meyer. "The ROBUR project: towards an autonomous flapping-wing animat ." *JournÃ©es MicroDrones* 3.3 (2004): 1-15. Print.

G C H E De Croon, M A Groen, C De Wagter, B Remes, R Ruijsink, and B W Van Oudheusden. "Design, aerodynamics and autonomy of the DelFly." *Bioinspiration & Biomimetics* 7.2 (2012): 025003. Print.

"GoPro | World's most Versatile Camera | HERO3+ Black Edition." *GoPro Official Website: The World's Most Versatile Camera*. GoPro, n.d. Web. 1 May 2014. <http://gopro.com/>.

Grauer, Jared A., and James E. Hubbard. "Multibody Model of an Ornithopter." *Journal of Guidance, Control, and Dynamics* 32.5 (2009): 1675-1679. Print.

"HobbyWing Platinum-80A-PRO Brushless ESC for Trex 500/550." *HobbyPartz*. HobbyPartz, n.d. Web. 1 May 2014. <http://www.hobbypartz.com/07e-c-platinum-80a.html>.

"Introducing CESÂ EduPack." *Granta Material Inspiration: Teaching resources for materials and process education*. Granta, n.d. Web. 1 May 2014. <http://www.grantadesign.com/education/edupack/index.htm>.

Karasek, Matej. "Robotic Hummingbird - Prototype Design." *Actives Structures Laboratory*. Universite Libre De Bruxelles, 23 Mar. 2011. Web. 1 May 2014. <http://scmero.ulb.ac.be/project.php?id=6&page=hummingbird_robot.html>.

Kim, Joong-Kwan, Jun-Seong Lee, and Jae-Hung Han. "Passive Longitudinal Stability in Ornithopter Flight." *Journal of Guidance, Control, and Dynamics* 35.2 (2012): 669-674. Print.

"LabVIEW System Design Software." *National Instruments*. National Instruments, n.d. Web. 1 May 2014. <http://www.ni.com/labview/>.

"MATLAB:Language of Technical Computing." *Products & Services: MATLAB*. MathWorks, Inc., n.d. Web. 1 May 2014. <http://www.mathworks.com/products/matlab/>.

Mueller, T. J. *Fixed and flapping wing aerodynamics for micro air vehicle applications*. Reston, Va.: American Institute of Aeronautics and Astronautics, 2001. Print.

"NI USB-6008 12-Bit, 10 kS/s Low-Cost Multifunction DAQ." *National Instruments*. National Instruments, n.d. Web. 1 May 2014. <http://sine.ni.com/nips/cds/view/p/lang/en/nid/201986>.

"Ornithopter Flight Dynamics and Control." *Morpheus Laboratory, University of Maryland*.

Uinversity of Maryland, n.d. Web. 28 Apr. 2014. <http://www.morpheus.umd.edu/research/flapping-wing-flight/ornithopter.html>.

Palmer, Robert. *Encyclopedia of Polymer Science and Technology*. Malden: John Wiley & Sons, Inc., 2001. Print.

Popovic, Marko B. *Biomechanics and robotics*. Stanford: Pan Stanford Publishing, 2013. Print.

"Tacon Big Foot 46 Brushless Out Runner Motor for Airplane (670KV)." *HobbyPartz*. HobbyPartz, n.d. Web. 1 May 2014. <http://www.hobbypartz.com/96m605-bigfoot46-4020-670kv.html>.

Wissa, A.A, Y Tummala, J E Hubbard Jr, and M I Frecker. "Passively morphing ornithopter wings constructed using a novel compliant spine: design and testing." *Smart Materials and Structures* 21.9 (2012): 094028. Print.

Appendix A: Raw Data Samples

Elapsed Time	Mass	Voltage Right	Voltage Left	Mass	Voltage Back
0.2	0	-0.693	-1.558	0	-0.823
0.3	0	-0.693	-1.573	0	-0.812
0.4	0	-0.683	-1.568	0	-0.812
0.8	0	-0.688	-1.563	0	-0.818
0.3	2.5	0.529	-0.336	3	0.731
0.4	2.5	0.529	-0.336	3	0.705
0.5	2.5	0.524	-0.341	3	0.715
0.7	5	1.649	0.973	6	2.172
0.8	5	1.659	0.998	6	2.167
0.1	5	1.644	0.973	6	2.162
0.2	5	1.649	0.973	6	2.182
0.7	7.5	2.805	2.348	9	3.603
0.8	7.5	2.805	2.353	9	3.619
0.9	7.5	2.825	2.373	9	3.598
1	7.5	2.845	2.378	9	3.664
0.1	7.5	2.795	2.332	9	3.568
0.1	10	3.991	3.555	12	5.121
0.2	10	3.991	3.57	12	5.08
0.3	10	3.991	3.565	12	5.085
0.4	10	4.006	3.585	12	5.085

Table 2: A sample of raw data from individual sensor calibration.

Elapsed Time	Weight Added (lb)	Voltage Right	Voltage Left	Voltage Back	Right Calibrated Voltage	Left Calibrated Voltage	Back Calibrated Voltage	Weight + Offset (lb)	Calibrated Sum of Weights (lb)
0.2	0	-0.232	0.07	-0.769	0.962244027	3.195630586	-0.116847249	2	4.041027364
0.3	0	-0.227	0.065	-0.769	0.972909556	3.185700099	-0.116847249	2	4.041762407
0.4	0	-0.227	0.055	-0.779	0.972909556	3.165839126	-0.138092203	2	4.000656479
0.5	0	-0.232	0.065	-0.769	0.962244027	3.185700099	-0.116847249	2	4.031096878
0.6	0	-0.232	0.07	-0.753	0.962244027	3.195630586	-0.082855322	2	4.075019291
0.7	0	-0.222	0.05	-0.774	0.983575085	3.15590864	-0.127469726	2	4.012013999
0.8	0	-0.227	0.055	-0.764	0.972909556	3.165839126	-0.106224772	2	4.032523911
0.9	0	-0.232	0.06	-0.774	0.962244027	3.175769613	-0.127469726	2	4.010543914
1	0	-0.227	0.065	-0.759	0.972909556	3.185700099	-0.095602294	2	4.063007361
0.1	0	-0.217	0.05	-0.794	0.994240614	3.15590864	-0.169959635	2	3.980189619
0.2	0	-0.227	0.045	-0.789	0.972909556	3.145978153	-0.159337157	2	3.959550552
0.3	0	-0.227	0.05	-0.769	0.972909556	3.15590864	-0.116847249	2	4.011970947
0.4	0	-0.222	0.035	-0.789	0.983575085	3.12611718	-0.159337157	2	3.950355108
0.5	0	-0.232	0.04	-0.789	0.962244027	3.136047666	-0.159337157	2	3.938954536
0.6	0	-0.227	0.05	-0.784	0.972909556	3.15590864	-0.14871468	2	3.980103516
0.7	0	-0.232	0.05	-0.774	0.962244027	3.15590864	-0.127469726	2	3.990682941
0.8	0	-0.222	0.045	-0.789	0.983575085	3.145978153	-0.159337157	2	3.970216081
0.9	0	-0.227	0.045	-0.789	0.972909556	3.145978153	-0.159337157	2	3.959550552
1	0	-0.227	0.05	-0.774	0.972909556	3.15590864	-0.127469726	2	4.00134847
0.1	0	-0.222	0.045	-0.779	0.983575085	3.145978153	-0.138092203	2	3.991461035
0.2	0	-0.211	0.05	-0.779	1.007039249	3.15590864	-0.138092203	2	4.024855686
0.3	0	-0.232	0.05	-0.774	0.962244027	3.15590864	-0.127469726	2	3.990682941

Table 3: A sample of raw data to calibrate the complete sensor array.

.

Appendix B: MATLAB Model

```
clc; clear; close all;
```

Theoretical Model

Ornithopter MQP

Slider Crank

```
%Parameters
a = 0.034925;          %1.375"
b = 0.1524;            %6"

%Input for the crank
t1 = [-pi:pi/20:3*pi]';
t1_dot = 25;                        %25rad/s = 240rpm

%Change in time
dt = pi/20/t1_dot;
time = zeros(length(t1),1);
t = dt;
for row = 2:length(t1)
   time(row) = t;
   t = t + dt;
end

%Equations
t2 = asin((-a/b)*sin(t1));
sliderPos = a.*cos(t1) + b.*cos(t2);
sliderVel = zeros(length(t1),1);
for row = 2:length(t1)
    sliderVel(row) = (sliderPos(row) - sliderPos(row-1))/dt;
end
```

```
%Transmission Angle
mu = acos((a/b)*sin(t1));


maxSlider = max(sliderPos);
minSlider = min(sliderPos);


%Parameter
c = 0.09271;          %3.65"


%Calculate change of angle for lever
beta = asin((sliderPos - (maxSlider - minSlider)/2 - minSlider)/c);
```

Double Rocker

```
r1 = 0.0635;          %2.5"
r2 = 0.087884;        %3.46"
r3 = 0.0508;          %2"
r4 = 0.0254*2;        %1"
theta1 = pi/6;
t2_initial = 60.73*pi/180;
theta2 = t2_initial + beta;
theta2_dot = zeros(length(t1),1);


%Calculate input
% for row = 2:length(t1)
%     theta2_dot(row) = (theta2(row) - theta2(row-1))/(sliderVel(row) - sliderVel(row-1))*sliderVel(row);
% end
theta2_dot = diff(theta2)./diff(time);


x3 = r1*cos(theta1) - r2*cos(theta2);
y3 = r1*sin(theta1) - r2*sin(theta2);


%Calculate joint position of the shoulder
theta4 = atan2(y3,x3) + acos((x3.^2 + y3.^2 + r4^2 - r3^2)./(-2*r4*sqrt(x3.^2 + y3.^2)));
theta4d = theta4*180/pi;
```

```
%Calculate theta3
num = (y3 + r4*sin(theta4))./r3;
den = (x3 + r4*cos(theta4))./r3;
theta3 = atan2(num, den);
```

Angular Velocity of shoulder joint

```
theta4_dot = zeros(length(t1),1);
% for row = 2:length(t1)
%     theta4_dot(row) = (theta4(row) - theta4(row-1))/(theta2(row)-theta2(row-1))*theta2(row);
% end
theta4_dot = [0;diff(theta4)./diff(time)];
theta4d_dot = theta4_dot*180/pi;
```

Plot Angular Position and Velocity

```
h1=figure;
subplot(2,1,1)
plot(time,theta4d, 'LineWidth',2)
title('\fontsize{16}Theoretical Wing Angular Position')
xlabel('\fontsize{14}Time [s]')
ylabel('\fontsize{14}Angular Position [degree]')

subplot(2,1,2)
plot(time,theta4d_dot,'LineWidth',2)
title('\fontsize{16}Theoretical Wing Angular Velocity')
xlabel('\fontsize{14}Time [s]')
ylabel('\fontsize{14}Angular Velocity [degree/sec]')
```

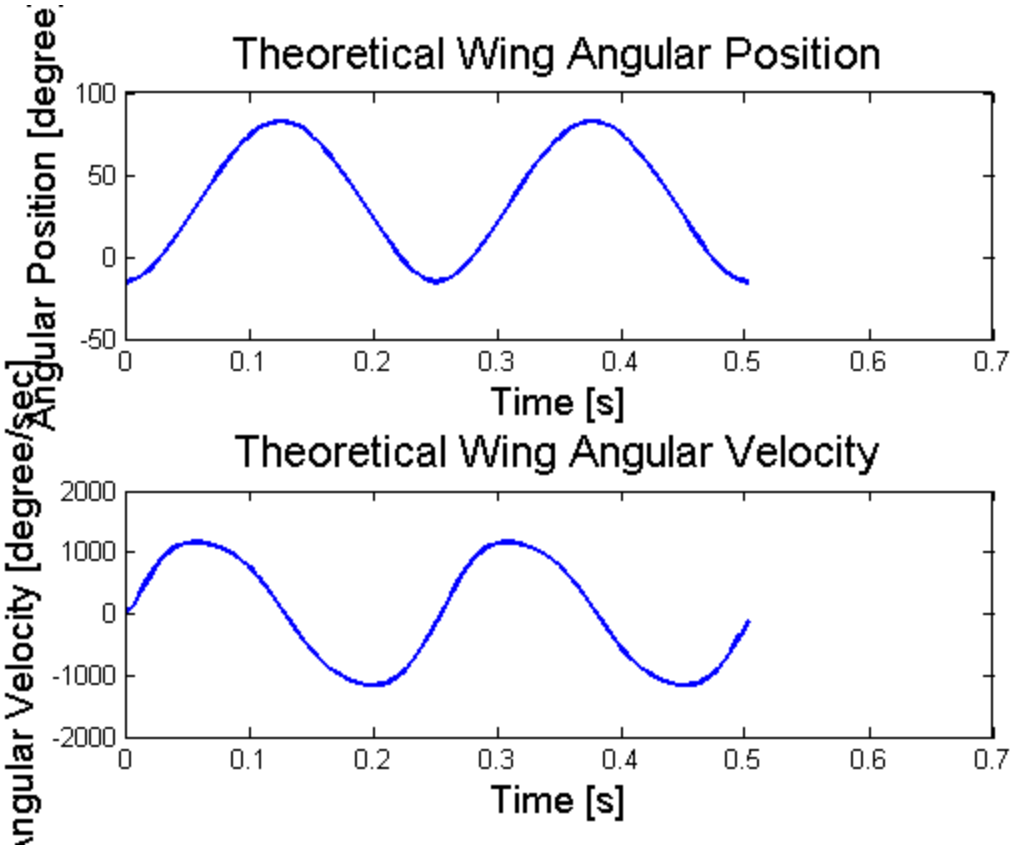

Force of Lift for both wings

$$F_{lift} = \frac{1}{3} C_d \rho W L^3 \cos^2 \gamma \sin \gamma \omega^2$$

```
%Parameters

Cd = 2;

rho = 1.1839;

W = 0.254;          %10in

L = 0.762;          %30in

gamma = pi/6;


wingBeatAmplitude = max(theta4) - min(theta4);


theta4_dot_mean = mean(theta4_dot(1:12,1))

flappingFreq = theta4_dot_mean/(2*wingBeatAmplitude)
```

```
F_lift = 1/3*Cd*rho*W*L^3*sin(2*gamma).*theta4_dot.^2;
Total_mean_F_lift = mean(F_lift)

F_drag = F_lift/tan(gamma);

MaxPower = max(F_drag)*max(theta4_dot)*2/3*L
% Power_mean = mean(Power(1:12,1))
```

```
theta4_dot_mean =

   13.7653


flappingFreq =

    4.0224


Total_mean_F_lift =

   16.8852


MaxPower =

  568.8748
```

Plot Force of Lift

```
h2=figure;
plot(time,F_lift,'LineWidth',2)
hold on;
plot(time,ones(length(F_lift),1)*mean(F_lift),'-r','LineWidth',2)
legend('Force', 'Average Force');
```

```
set(legend);
title('\fontsize{16}Theoretical Force of Lift');
xlabel('\fontsize{14}Time [s]');
ylabel('\fontsize{14}Force of Lift [N]');
```

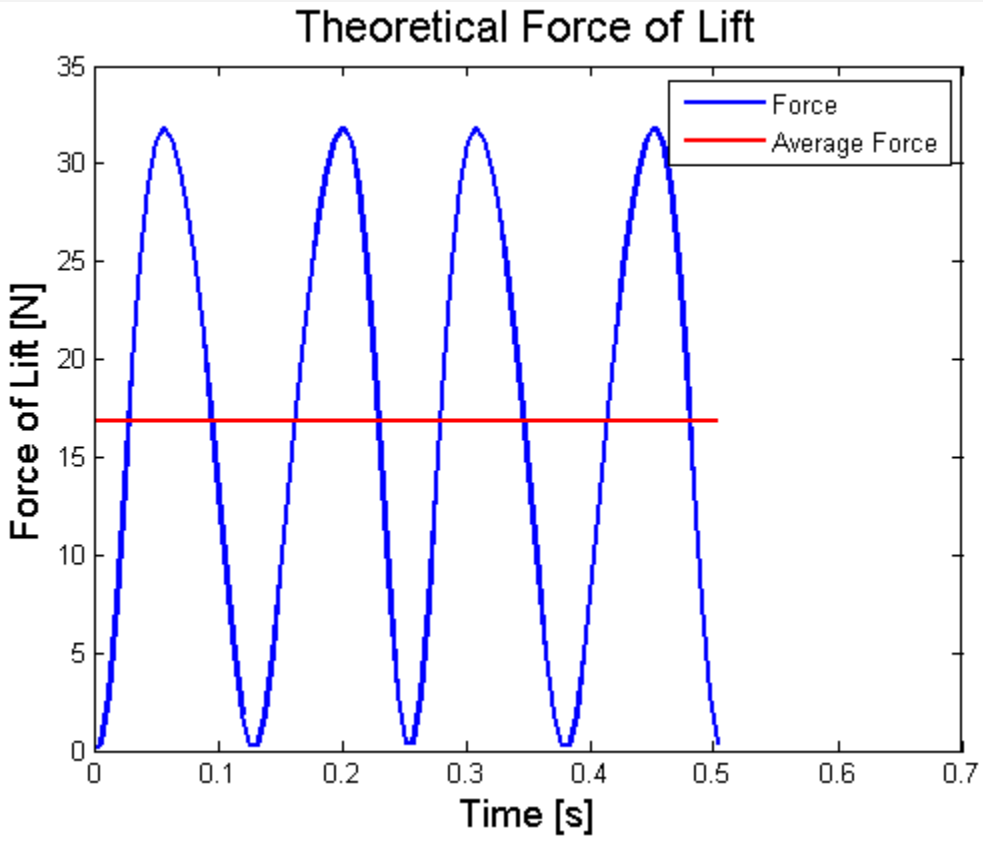

Published with MATLAB® R2013a

Appendix - Model Derivation

1 Slider Crank Mechanism

The first mechanism used is a slider-crank four bar mechanism. Figure 1 shows a schematic diagram of a slider crank mechanism and the common notation for the different components. In order to evaluate this linkage, the mechanism can be broken up into multiple vectors and a close loop. Utilizing this loop, we can derive X and Y components.

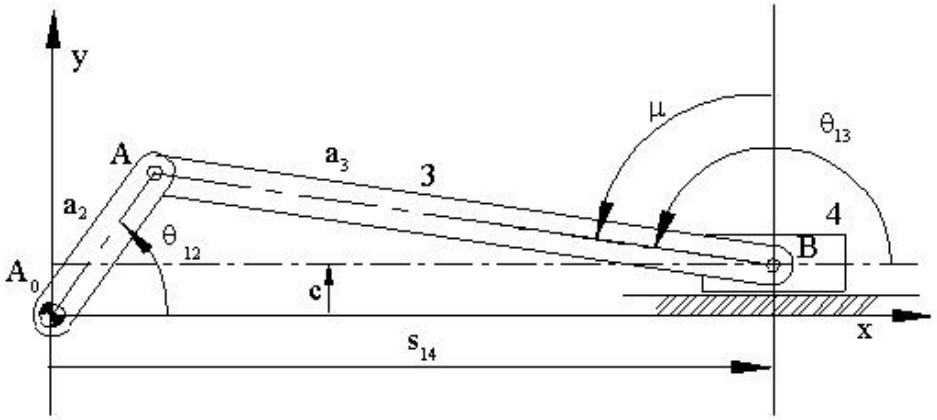

Figure 1: Slider-Crank mechanism with vector loops and basic parameters.

1.1 Position Analysis

The vector equations for the X and Y directions are given respectively based on the loop-closer equations.

$$a\cos\theta_1 + b\cos\theta_2 = x \tag{1}$$

$$a\sin\theta_1 - b\sin\theta_2 = 0 \tag{2}$$

The position of the slider at any given position of the crank is given by (1). From (2), the position of the linkage can be described. Looking closely to (1) and (2), it is a 2 equations and 2

unknown system that can derive the slider position and θ_2. θ_2 is easily calculated from (2). From (3), the slider position can be easily calculated from (1).

$$\theta_2 = \arcsin\left(-\frac{a}{b}\sin\theta_1\right) \tag{3}$$

The transmission angle is used to evaluate the amount of power transferred from the crank to the output and can be found from the following relationship as seen in Equation (4). The maximum and minimum transmission angles are found when the crank is perpendicular to the slider.

$$\mu = \arccos\left(\frac{a}{b}\sin\theta_1\right) \tag{4}$$

$$\cos\mu_{max} = \frac{a}{b}$$

$$\cos\mu_{min} = -\frac{a}{b}$$

The maximum and minimum transmission angles occur at $\theta_1 = 0$, and $\theta_1 = \pi$ respectively.

1.2 Velocity Analysis

For the Slider-Crank Mechanism shown in Figure , the velocity of the slider can also be calculated as a function of the crank angle. Using the chain rule of differentiation, the velocity is given by the following equation. Note that the velocity for the rest of the components will be found in a similar fashion. The velocities will be computed numerically, therefore, an analytical solution will be in terms of $theta_1$.

$$\dot{x} = \frac{\partial x}{\partial t} = \frac{\partial x}{\partial \theta}\cdot\dot{\theta}_1$$

$$\dot{x} = -\dot{\theta}_1 \left(a \sin\theta_1 + \frac{a^2 \cos\theta_1 \sin\theta_1}{b\left(1 - \frac{a^2 \sin{\theta_1}^2}{b^2}\right)^{\frac{1}{2}}} \right) \tag{5}$$

By having the slider position as a function of the crank speed, the velocity analysis can be carried forward to the end effector, in our case, the wings.

2 Lever from Slider-Crank to Double-Rocker Mechanism

This lever takes the linear motion of the Slider-Crank and converts it to the input of the Double-Rocker Mechanism seen earlier. This simple mehanism rotates around a pin and allows to transfer the linear motion into a rocking action due to the pin on the eslider. Figure 2 shows the schematics of the lever and the maximum motion allowed.

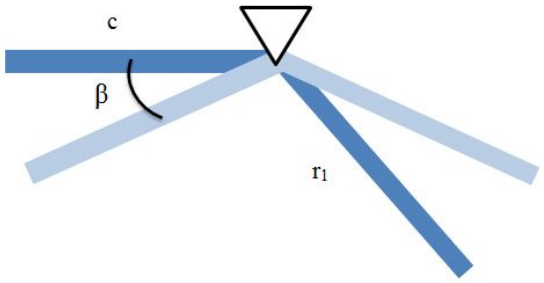

Figure 2: Coupling of slider to rocker in the form of lever.

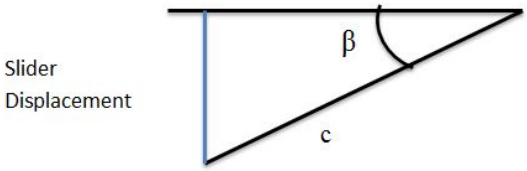

Figure 3: Trigonometric relation of maximum rocking based on slider motion

Let's denote an angle beta such that it changes with the position of the slider and c the lever arm.

$$\beta = \arcsin\left(\frac{\bar{x} + x_{min} - x_{actual}}{c}\right) \tag{6}$$

By calculating β, we can measure the angle θ_2, the input of the double-rocker. When $\beta = 0$, the $\theta_{2,o}$ describes the initial position of the mechanism.

$$\theta_2 = \theta_{2,o} - \beta \tag{7}$$

3 Double Crank Four Bar Linkage

The Four bar linkage, as shown in Figure 4, can be analyzed using a close-loop vector equation in the complex plane. Our mechanism will create a Double-Rocker due to the link parameters. This mechanism allows rocking the wing shoulders back and forth, creating the wing motion.

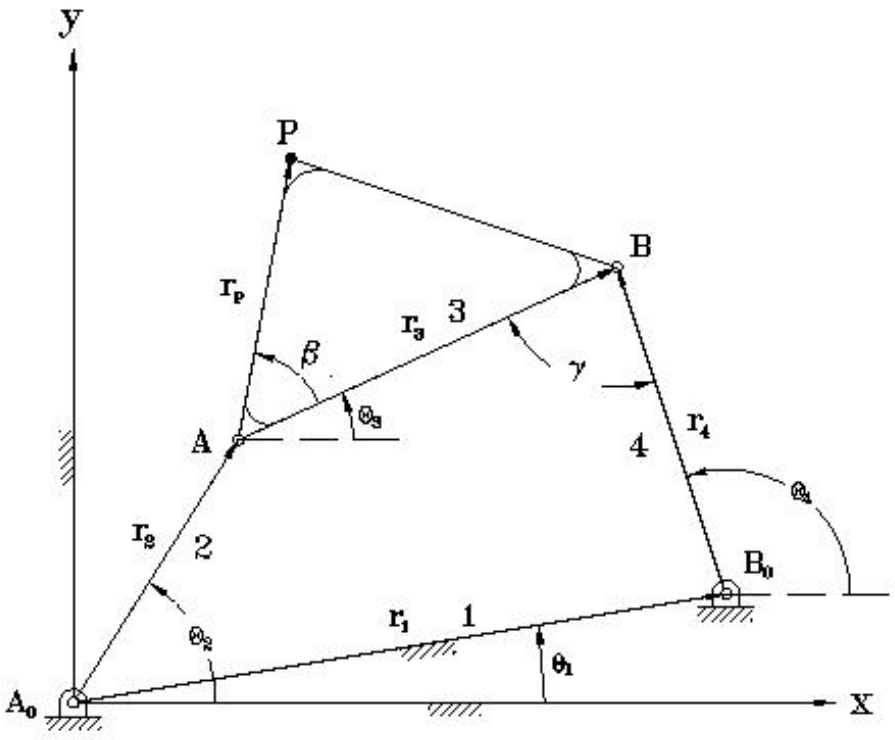

Figure 4: Cross-sectional view of wing including forces acting on it.

3.1 Position Analysis

In order to analyze the position and velocity of the mechanism, a vector approach using complex numbers will be used. A close loop equation of each link can be found to be as follows.

$$r_2 \exp(i\theta_2) + r_3 \exp(i\theta_3) = r_1 \exp(i\theta_1) + r_4 \exp(i\theta_4) \tag{8}$$

Let,

$$z = (x_3, y_3) = r_1 \exp(i\theta_1) - r_2 \exp(i\theta_2) \tag{9}$$

Where z can be divided into its real and imaginary components (x_3, y_3),

$$x_3 = r_1 \cos\theta_1 - r_2 \cos\theta_2$$

$$y_3 = r_1 \sin\theta_1 - r_2 \cos\theta_2$$

Substituting (9) into (8) yields

$$r_3 \exp i\theta_3 - r_4 \exp i\theta_4 = z \tag{10}$$

Then, the real and imaginary components are separated from (10) into

$$cos\theta_3 = \frac{x_3 + r_4 \cos\theta_4}{r_3} \tag{11}$$

$$sin\theta_3 = \frac{y_3 + r_4 \sin\theta_4}{r_3} \tag{12}$$

Substituting (11) and (12) into

$$\sin\phi^2 + \cos\phi^2 = 1$$

We obtain

$$y_3 \sin\theta_4 + x_3 \cos\theta_4 = \frac{x_3^2 + y_3^2 + r_4^2 - r_3^2}{-2 \cdot r_4} \tag{13}$$

Using the Amplitude-Phase form, θ_4 can be derived. The Amplitude-Phase form is given by (14).

$$A\cos(\theta_4 + \phi) = C_1 \sin\theta_4 + C_2 \cos\theta_4 \tag{14}$$

where $A = \sqrt{C_1^2 + C_2^2}$ and $\phi = \arctan(C_2/C_1)$.

Therefore,

$$\sqrt{x_3^2 + y_3^2} \cdot \cos(\theta_4 + \phi) = \frac{x_3^2 + y_3^2 + r_4^2 - r_3^2}{-2 \cdot r_4}$$

$$\theta_4 = \arctan\left(\frac{y_3}{x_3}\right) \pm \arccos\left(\frac{x_3^2 + y_3^2 - r_4^2 - r_3^2}{-2 \cdot r_3 \sqrt{x_3^2 + y_3^2}}\right)$$

As θ_4 is known, dividing (11) by (12),

$$\tan\theta_3 = \left(\frac{\frac{y_3 + r_4 \sin\theta_4}{r_3}}{\frac{x_3 + r_4 \cos\theta_4}{-r_4}}\right) \tag{15}$$

Therefore, θ_3 can be obtained

$$\theta_3 = \arctan\left(\frac{\frac{y_3 + r_4 \sin\theta_4}{r_3}}{\frac{x_3 + r_4 \cos\theta_4}{-r_4}}\right) \tag{16}$$

4 Aerodynamic Force of Lift

The wings was modeled as a flat plate as shown in Figure 5 above. In order to simplify calculations, assumptions that the wing will remain rigid throughout its motion, and have a constant angle of attack γ. The basic equation for aerodynamic drag for a flat plate is given by in (17) below.

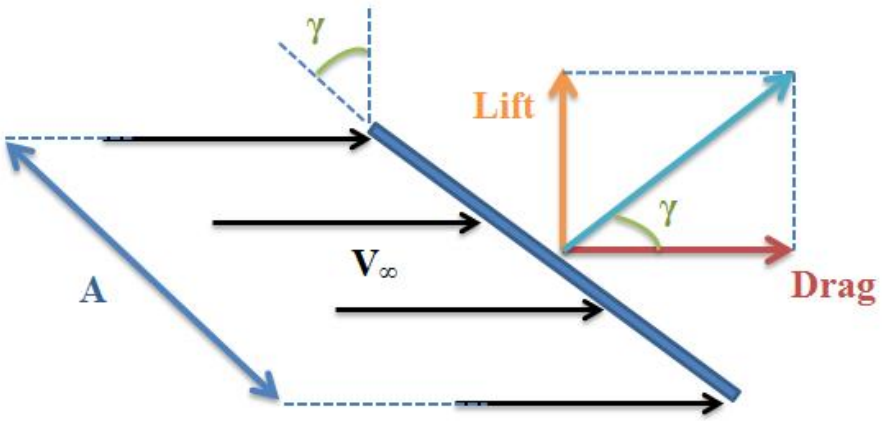

Figure 5: Cross-sectional view of wing including forces acting on it.

$$F_D = \frac{1}{2}\rho\, v^2 C_D A \tag{17}$$

Where ρ is the density of air, v is the air velocity in the wing motion direction, C_D is the coefficient of drag, and A is the cross-sectional area of the wing. As the angular velocity is a function of the length of the wing, then

$$Av = W\omega\cos\gamma\int_0^L x\,\mathrm{d}x \tag{18}$$

$$Av = \frac{1}{3}L^3 W\,\omega^2 cos^2\gamma \tag{19}$$

Substituting (19) into (17),

$$F_D = \frac{1}{6}\rho\, C_d L^3 W\,\omega^2\, cos^2\gamma \tag{20}$$

By simple trigonometry, as seen in Figure 5, the Lift and Drag are related by $\tan\gamma$.

$$\frac{F_L}{F_D} = \tan\gamma$$

$$F_L = \frac{1}{6}\rho\, C_D L^3 W\,\omega^2 \cos(\gamma)\,\sin(\gamma) \tag{21}$$

Substituting $2\sin\gamma\cos\gamma = \sin(2\gamma)$

$$F_L = \frac{1}{12}\rho C_D L W^3 \omega^2 \sin(2\gamma) \tag{22}$$

Finally, (22) denotes the lift force produced by one wing during its flapping motion. This result should be doubled in order to account for the two flapping wings.

5 Power Requirements

The power requirements of the system will be approximated to be equal to the output of the system. Therefore the power output of the system will be based on the torque created by the force of drag acting on the wing and the angular acceleration of the wing. The force of drag will be acting on the centroid of the force distribution on the wing.

$$P = \tau \cdot \omega = F \cdot v \tag{23}$$

$$\tau = F_D \times r_p = F_D \left(\frac{2}{3}L\right) \tag{24}$$

Substituting (24) into (23), we obtain

$$P = \frac{2}{3} F_D L \dot{\theta}_4 \tag{25}$$